SAND2017-2878J

Quantifying Hyporheic Exchanges in a Large Scale River Reach Using Coupled 3-D Surface and Subsurface Computational Fluid Dynamics Simulations

J. Bao[1], T. Zhou[1], M. Huang[1], Z. Hou[1], W. Perkins[1], S. Harding[1], S. Titzler[1], G. Hammond[2], H. Ren[1], P. Thorne[1], S. Suffield[1], C. Murray[1], J. Zachara[1]

[1]Pacific Northwest National Laboratory, Richland, WA, USA

[2]Sandia National Laboratories, Albuquerque, NM, USA

Abstract

Hyporheic exchange is a critical mechanism shaping hydrological and biogeochemical processes along a river corridor. Recent studies on quantifying the hyporheic exchange were mostly limited to local scales due to field inaccessibility, computational demand, and complexity of geomorphology and subsurface geology. Surface flow conditions and subsurface physical properties are well known factors on modulating the hyporheic exchange, but quantitative understanding of their impacts on the strength and direction of hyporheic exchanges at reach scales is absent. In this study, a high resolution computational fluid dynamics (CFD) model that couples surface and subsurface flow and transport is employed to simulate hyporheic exchanges in a 7-km long reach along the main-stem of the Columbia River. Assuming that the hyporheic exchange does not affect surface water flow conditions due to its negligible magnitude compared to the volume and velocity of river water, we developed a one-way coupled surface and subsurface water flow model using the commercial CFD software STAR-CCM+. The model integrates the Reynolds-averaged Navier-Stokes (RANS) equation solver with a realizable $k-\varepsilon$ two-layer turbulence model, a two-layer all y^+ wall treatment, and the volume of fluid (VOF) method, and is used to simulate hyporheic exchanges by tracking the free water-air interface as well as flow in the river and the subsurface porous media. The model is validated against measurements from acoustic Doppler current profiler (ADCP) in the stream water and hyporheic fluxes derived from a set of temperature profilers installed across the riverbed. The validated model is then employed to systematically investigate how hyporheic exchanges are influenced by surface water fluid dynamics strongly regulated by upstream dam operations, as well as subsurface structures (e.g. thickness of riverbed and subsurface formation layers) and hydrogeological properties (e.g. permeability). The results suggest that the thickness of riverbed alluvium layer is the dominant

factor for reach-scale hyporheic exchanges, followed by the alluvium permeability, the depth of the underlying impermeable layer, and the assumption of hydrostatic pressure.

1. Introduction

In a hyporheic zone, water is exchanged laterally or beneath the stream channel with saturated sediments (Findlay, 1995). Hyporheic exchange can potentially change stream water chemistry through biogeochemical reactions and transport such as carbon and nitrogen cycling, and biodegradation of organic contaminates (Findlay *et al.*, 1993; Findlay, 1995; Valett *et al.*, 1996; Sobczak and Findlay, 2002; Anderson *et al.*, 2005; Zarnetske *et al.*, 2011a; Zarnetske *et al.*, 2011b). Essentially governed by permeability of sediments and local hydraulic gradients, the hyporheic flow dynamics are influenced by many factors, such as channel geometry, aquifer thickness, and hydrology in both space and time (Brunke and Gonser, 1997; Winter, 1999). The hydraulic gradient across the river bed is time-varying, and highly depends on river stage variations. For a dam-regulated river, upstream dam operations could dramatically impact river stage variations on a wide temporal spectrum from hourly to monthly (Poff *et al.*, 1997), and at a spatial scale extending to a few hundred kilometers downstream of the dam (Arntzen *et al.*, 2006). Although more than 30,000 large dams were built globally in the past 50 years, resulting in surface water systems considerably affected by the dams (Vörösmarty and Sahagian, 2000; Hanasaki *et al.*, 2006; Zhou *et al.*, 2016), reach-scale hyporheic exchange dynamics over space and time for highly regulated large rivers have not been adequately studied.

The Columbia River is the largest river in the Pacific Northwest region of North America. Its drainage basin is about 668,000 km^2 and extends into seven U.S. states and a Canadian province. Figure 1(a) shows the section of Columbia River in the Washington State. The Hanford Site is a mostly decommissioned nuclear production complex in USA built along the Columbia River in Washington State. After the Cold War, the decades of manufacturing of nuclear weapons left

behind 200,000 m^3 of high-level radioactive waste stored within 177 storage tanks, which are almost all located in Hanford 300A area as yellow box marked in Figure 1. Understanding the dynamics of hyporheic exchange in this area is thus critical to the health of downstream ecosystems and human settlements.

Quantifying hyporheic fluxes in a regulated large river reach is challenging given the size of the domain. The existing field measurement methods mainly include direct measurements, indirect measurements based on the Darcy's Law, mass balance, and heat transport equations (Kalbus *et al.*, 2006). These measurement methods often provide data at a point or over a very small area, therefore require a large number of measurement points to be representative of the reach, which is labor intensive and physically challenging. Numerical simulations thus become effective alternatives.

Lane et al. (Lane *et al.*, 1999) demonstrated the advantages of modeling the impact of fluvial geomorphology using a computational fluid dynamics (CFD) approach over the shallow water equations by applying the Reynold-averaged Navier-Stokes (RANS) equation to study two-dimensional and three-dimensional flow in a natural river channel (Keylock *et al.*, 2012). Applications of CFD modeling on flow and transport in natural river channels have emerged dramatically in the last decade as a result of improvement in computing power (Keylock *et al.*, 2012), but most of the successful studies focused on small to medium scale natural river channels or experimental river channels in laboratory settings, with dimensions of the channels a few meters in width, and up to a few hundred meters in length (Yazdi *et al.*, 2010; Constantinescu *et al.*, 2011;

Zhou and Endreny, 2013). For large-scale river reaches, given limitations in computational resources, most studies prefer the use of shallow water equations by assuming that the vertical length scale is much smaller than the horizontal length scale, and that the pressure field is hydrostatic (Banda and Seaid, 2012). The full three-dimensional CFD applications to large scale river channels that are a few hundred meters in width and a few kilometers in length are absent.

For large rivers, the surface water elevation plays an important role in driving the hyporheic exchange. Hence, it is critical to tracking the water-air interface in CFD models. Several multi-phase CFD models have been developed for this purpose, such as the multi-phase lattice Boltzmann method (LBM) (Donath *et al.*, 2010; Bao and Schaefer, 2013), the volume of fluid (VOF) method (Yazdi *et al.*, 2010), and the smooth particle hydrodynamics (SPH) method (Kazemi *et al.*, 2016). LBM and SPH intrinsically are powerful in multi-phase fluid dynamics, but are not computational efficient for bathymetries with large aspect ratios commonly found in large river reaches. Among these methods, VOF is more popular for simulating free surfaces in river channels, because it can be used in conventional finite volume and finite difference CFD solvers and compatible with unstructured and adaptive meshes, therefore is computationally more efficient for domains of large-aspect ratios.

In simulations of flow underneath the riverbed of large river reaches, it is common to use hydrostatic pressure on the river bed as boundary conditions, by neglecting the pressure induced by the river water fluid dynamics (Chen *et al.*, 2012; Chen *et al.*, 2013). However, lab-scale experiments and corresponding CFD simulations indicated that the fluid dynamics could lead to

enhanced hyporheic fluxes (Zhou and Endreny, 2013), suggesting that dynamical effects should not be neglected. Studies that assessing the impact of fluid dynamics on hyporheic flux simulations and for suggesting scales at which the pressure induced by river water fluid dynamics can be ignored are very limited.

In addition, magnitudes and directions of hyporheic fluxes across the riverbed are governed and modulated by a variety of factors, such as flow conditions, subsurface structure and properties. The flow conditions are strongly regulated by upstream and downstream hydroclimatic conditions that provide lateral boundary conditions to the problem. The subsurface structure and properties assigned to the domain are highly heterogeneous in nature and subject to a large degree of uncertainties (Hartman and Dresel, 1998).

To address these issues in a computationally efficient way, a one-way coupled surface water and subsurface three-dimensional CFD simulation model was built using the commercial CFD software STAR-CCM+ for studying surface water dynamics and hyporheic exchanges over a 7-km section along the main-stem of the Columbia River. Using this model, we aim to establish a tool capable of quantifying spatial and temporal dynamics of hyporheic exchanges over a large scale river reach in a mechanistic way, by validating it against in-stream flow velocity and point flux measurements, and exploring the modulating factors and the rank of their significance using the validated model. In section 2, the study domain and its characteristics are introduced. Section 3 describes CFD model configuration and coupling strategy between the surface and subsurface domains, and methods for analyzing the sensitivity of subsurface properties and dynamical versus

130 hydrostatic pressures on hyporheic fluxes. The results, including model validations and sensitivity
131 analyses are discussed in Section 4.

132

133 ## 2. Description of the study domain and dataset

134 The 7-km modeling domain is shown as the red box in Figure 1(a). The inserted small figures in
135 Figure 1(a) show the location of this 7-km reach in the context of the Washington State and the
136 Hanford site. Elevations at the riverbed were collected from Light Detection And Ranging (LiDAR)
137 surveys at 1-m resolution (Coleman *et al.*, 2010) and used to inform the bathymetry in the CFD
138 model setup. The ADCP measurements were carried out at four transects over the study reach on
139 19 Febuary 2016 (green lines in Figure 1(a)). The measurements were used to validate the CFD
140 model for surface water velocities. These transects were selected to cover the entire channel width
141 (transect C), main channel with deep bathymetry and relatively high flow velocity (transects A and
142 D), and secondary channel with shallow bathymetry and lower flow velocity (transect B). A vessel
143 mounted 1200 kHz RDI Workhorse Sentinel ADCP was used to measure the flow velocity profiles
144 with a 0.5-m vertical interval and 0.2-Hz output frequency. Measurements at each transect were
145 repeated twice and the total discharge between the pair measurements were compared and
146 confirmed to be consistent within the 10% error range. The five red triangles in Figure 1(a) mark
147 the iButton® locations. The iButton sensor is a cylindrical, wireless device with a 17 mm diameter
148 and 6 mm in thickness. Its data storage capacity is 4096 values with a 0.0625 °C measuring
149 resolution and 0.5 °C in accuracy. At each location, two sensors were secured in separate open
150 drill holes 10 cm above and below river bed in a solid plastic rod with one inch in diameter, and
151 1.53 m in length half planted in the river bed. All sensors were programmed to record every 10
152 minutes from 2 March 2016 to 30 March 30 2016. We estimated vertical hyporheic fluxes at these

iButton monitoring sites using the method that combines a Maximum Likelihood estimator (LPML) developed by Vandersteen et al. (Vandersteen *et al.*, 2015), a 1-D heat transfer model described in Turcotte and Schubert (Turcotte and Schubert, 1982), and a regression relationship between flow conditions and hyporheic fluxes (Zhou *et al.*, 2017a; Zhou *et al.*, 2017b). The indirectly measured hyporheic fluxes from iButtons were used to validate the simulated ones. The white dot is an inland well, which records the subsurface water level used for initial and boundary conditions in the CFD simulations.

The Columbia River flows from north to south through the study reach over an unconfined aquifer on top of the impermeable Columbia River Basalt Group. The aquifer has a thickness ranging from 20 to 60 m, and contains two major hydrogeological units: the highly permeable Pleistocene flood gravel layer of the Hanford Formation on the top, and a more consolidated and less permeable Miocene to Pliocene fluvial deposition layer of the Ringold Formation at the bottom (Hartman and Dresel, 1998). At the very top of the river bed, there exists a thin alluvium with varying thicknesses ranging from 1 to 3 m. In this study, the subsurface structure was simplified into four layers as shown in Figure 1(b). The alluvium layer is assumed to be ~2 m, and its horizontal permeability k_H^A is estimated from underwater video-camera footage and accompanying grain-size analyses (Fritz and Arntzen, 2007). The distribution of k_H^A is shown in Figure 1(c). The ratio between vertical (k_V^A) and horizontal (k_H^A) permeability of the alluvium layer is 0.1, and porosity is 0.17. The Hanford layer is assumed to lay underneath the alluvium layer, and extends to 98 m above the sea level, while the river bed is ~100 m above the sea level based on the North American Vertical Datum of 1988 (NAD88). The horizontal permeability of the Hanford layer (k_H^H) is $1.23 \times 10^{-8}\ m^2$. The ratio between vertical (k_V^H) and horizontal (k_H^H) permeability of the Hanford layer

176 is 0.1, and porosity is 0.373. The Ringold gravel layer is underneath the Hanford layer, and extends
177 to 78 m above the sea level, where the horizontal (k_H^{RG}) permeability of the Ringold gravel layer
178 is $1.93 \times 10^{-9}\ m^2$. The ratio between vertical (k_V^{RG}) and horizontal (k_H^{RG}) permeability of the
179 Ringold gravel layer is 0.35, and porosity is 0.294. The Ringold lower mud layer is underneath the
180 Ringold gravel layer, where its horizontal permeability (k_H^{RM}) is $2.527 \times 10^{-15}\ m^2$. The ratio
181 between the vertical (k_V^{RM}) and horizontal (k_H^{RM}) permeability of the Ringold lower mud layer is
182 0.27, and porosity is 0.351. This subsurface structure and properties defined based on the available
183 characterization data of the Hanford site (Newcomb and Brown, 1961; Newcomb *et al.*, 1972;
184 Thorne *et al.*, 2006; Williams *et al.*, 2008; USDOE, 2010; Zachara *et al.*, 2012), are used to set up
185 the control case in this study and listed in Table I. The methodology for sensitivity analysis of the
186 subsurface properties is introduced in Section 3.2, and the results are discussed in Section 4.

187

188 ## 3. Methodology

189 ### 3.1 CFD model and coupling procedure

190 STAR-CCM+ CFD software (CD-adapco, 2015) was used for three-dimensional surface and
191 subsurface flow simulations. The numerical model involves solving the mass and momentum
192 conservation equations for fluid dynamics. The mass conservation equation is

$$\frac{\partial \rho}{\partial t} + \nabla \cdot (\rho \vec{v}) = 0, \tag{1}$$

193 where ρ is the fluid density, $\vec{v}$ is the velocity vector, and t is time. With Boussinesq hypothesis
194 (Schmitt, 2007), the RANS (O.Reynolds, 1895) momentum equation is in the form of

$$\frac{\partial (\rho \vec{v})}{\partial t} + \nabla \cdot (\rho \vec{v} \vec{v}) = -\nabla p - \nabla \cdot [\mu (\nabla \vec{v} + \nabla \vec{v}^T)] + \rho \vec{g}, \tag{2}$$

where p is pressure, $\vec{g}$ is gravity acceleration, and μ is effective viscosity, which can be calculated as

$$\mu = \mu_m + \mu_t. \quad (3)$$

μ_m is molecular dynamic viscosity, and μ_t is turbulent viscosity. In this study, for acquiring the flexibility on the mesh, the realizable $k-\varepsilon$ two-layer turbulence model and two-layer all y^+ wall treatment are used (Versteeg and Malaasekera, 1995; Liu *et al.*, 2012; CD-adapco, 2015). Therefore μ_t is calculated by a blending function as follows:

$$\mu_t = \lambda \mu_t|_{k-\varepsilon} + (1-\lambda)\mu_t|_{two-layer}. \quad (4)$$

$\mu_t|_{k-\varepsilon}$ is turbulent viscosity derived from the realizable $k-\varepsilon$ model (Shih *et al.*, 1995), and $\mu_t|_{two-layer}$ is turbulent viscosity derived from a two-layer formulation through the Wolfstein model (Wolfstein, 1969). λ is a blending factor, which is a function of wall distance Reynolds number (Jongen, 1998). The VOF model is applied for simulating and tracking the water-air interface:

$$\frac{\partial \alpha_w}{\partial t} + \nabla \cdot (\vec{v}\alpha_w) = 0, \quad (5)$$

where α_w is the water volume fraction. The fluid density ρ and molecular dynamic viscosity μ_m become

$$\rho = \alpha_w \rho_w + (1-\alpha_w)\rho_a \ , \quad (6)$$

$$\mu_m = \alpha_w \mu_{mw} + (1-\alpha_w)\mu_{ma} \ , \quad (7)$$

where ρ_w is water density, ρ_a is air density, μ_{mw} is water molecular dynamic viscosity, and μ_{ma} is air molecular dynamic viscosity.

In the subsurface domain, because the magnitude of velocities is very small, by adding a large viscous resistance term for subsurface porous media, the momentum equation (2) is simplified to (Huang and Ayoub, 2006)

$$\nabla p = -\bar{\bar{R}}_v \vec{v} \tag{8}$$

$\bar{\bar{R}}_v$ is the viscous porous resistance tensors. For the subsurface domain, it can be assumed as

$$\bar{\bar{R}}_v = \begin{bmatrix} \frac{\mu_m}{k_H} & 0 & 0 \\ 0 & \frac{\mu_m}{k_H} & 0 \\ 0 & 0 & \frac{\mu_m}{k_V} \end{bmatrix} \tag{9}$$

k_H and k_V are the horizontal and vertical permeability respectively.

The simulation domain is divided into two sub-domains: the surface flow region and the subsurface flow region, which share the river bed surface as the interface. For a given set of boundary conditions, including the upstream river stage, averaged upstream river water velocities, the downstream river stage, the model spins up surface water dynamics to an equilibrium state by assuming the riverbed as a non-penetrable wall. The pressure field at the river bed surface (Figure 1(d)) and VOF field are then extracted from the surface flow region and applied to the subsurface flow domain as the upper boundary condition. By applying the pressure and VOF boundary conditions on the river bed, the velocity, pressure, and VOF in the subsurface flow region can be solved by Eqs. (1), (5) and (8). Meanwhile, flow velocities across the river bed can be solved as well in the subsurface region, and an instantaneous map of simulated hyporheic fluxes on the river bed is shown in subsurface flow region in Figure 1(d). This coupling strategy is therefore a one-way coupling approach because fluxes on the river bed are not fed back into the surface flow region

to inform its simulation. There are two main reasons to using the one-way coupling. Firstly, the magnitude of the hyporheic flux ($\sim 1 \times 10^{-6}\ m/s$) is negligible, compared to the velocity of surface water ($\sim 1\ m/s$) in the river channel. Secondly, the turbulent flow velocity profile near the river bed in the surface flow region is derived from the turbulence wall function (Versteeg and Malaasekera, 1995; Liu *et al.*, 2012; CD-adapco, 2015) instead of using the simple Dirichlet boundary condition at the river bed. However, the available wall functions cannot handle the situation when the flux penetrates the boundary wall.

The CFD meshes were generated in STAR-CCM+. As shown in Figure 2, the orange region is the surface water domain for simulating river surface water, air, and the water-air interface. It contains 6.5 million cells. The grey region is the subsurface domain, which contains 8.6 million cells. It is worth mentioning that the vertical direction (z) is scaled up 10 times in order to show the mesh clearly in Figure 2. The horizontal resolutions of the meshes vary from 1 m to 25 m. In the surface water domain, 35 meshes of prism layers were used to discretize the sub-domain above the river bed, as illustrated in Figure 2(b), with distances of ~ 0.25 m to 0.45 m in the vertical direction. The rest of the surface water domain above the prism layers was discretized into five layers of thin meshes as shown in Figure 2(b), with a vertical resolution of ~1.5 m. In the subsurface domain, the meshes were extruded from the river bed to 50 m from the river bed by applying a hyperbolic tangent profile in the vertical direction with distances from 0.03 m to 3 m, as shown in Figure 2(b).

3.2 Sensitivity analyses

The hyporheic flux on the river bed is governed and affected by a variety of factors. We classify these factors into three categories: (1) surface flow and subsurface hydrologic conditions, (2) subsurface structure and properties, and (3) the hydrostatic pressure assumption in surface water.

3.2.1 Hydrologic conditions

The hydrologic conditions are strongly regulated by upstream and local hydroclimate including hydropeaking events created by dam operations (Hancock, 2002). The surface flow discharge and inland water level are the two key factors in characterizing the hydrologic condition, both of which are characterized by strong temporal variability. We evaluate the impact of these factors by randomly picking 50 flow conditions from the historical records in the period of 2008 to 2014, as shown in Table II. To make the discharge conditions appropriate for being used as boundary conditions to the CFD model, the river discharge were converted to upstream and downstream river stages, and averaged upstream velocities by using a one-dimensional hydrodynamic model, the Modular Aquatic Simulation System (MASS1) (Richmond and Perkins, 2009; Niehus *et al.*, 2014). MASS1 simulates steady and unsteady flow in rivers and canals by solving the one-dimensional, cross-section averaged equations of mass and momentum conservations (i.e., the St. Venant equations). MASS1 simulation results have been applied to various problems in the Columbia River basin with relatively high accuracy in predicting flow stage profiles along the Hanford Reach, with a mean absolute error (MAE) less than 0.15 m and a bias less than 0.06 m against field measurements (Tiffan *et al.*, 2002; McMichael *et al.*, 2003). The inland well water table was converted to subsurface water stages at north and south boundaries of the CFD domain. Figure 3 shows the comparison between the cumulative distribution functions (CDF) of the six hourly variables simulated by MASS1 and the 50 randomly selected flow conditions used as

boundary conditions to the CFD simulations. It is evident from the figure that the selected flow conditions are representative of the historical records.

3.2.2 Subsurface structure and properties

The structure and properties of the four layers in the subsurface domain is subject to a significant amount of uncertainties in terms of their depths and properties. Given that the CFD simulations are computationally expensive, especially given the number of scenarios to be considered, we selected a few combinations of the alluvium and subsurface properties to understand the sensitivity of simulated hyporheic fluxes to these factors. Specifically, we picked the alluvium layer thickness, alluvium layer permeability, and the depth to Ringold lower mud layer as the three key factors based on the uncertainty and spatial variability of these structural and physical attributes, and their critical control on hyporheic exchange as reported in literature (Fritz and Arntzen, 2007; Fritz *et al.*, 2007). Field survey shows that the recent riverbed alluvium is about a couple of meters thick, therefore in the baseline control case, alluvium layer thickness is assumed to be 2 m, and in the numerical experiments, the alluvium thickness is allowed to vary between 1-3 meters. As mentioned in Section 2, the baseline control case alluvium layer permeability k_H^A was estimated from underwater video-camera footage and accompanying grain-size analyses (Fritz and Arntzen, 2007). Assuming a medium level of heterogeneity, the low and high permeability scenarios are assumed to have an effective permeability adjustment between $k_H^A \times 1.648$ and $k_H^A/1.648$, which are equivalent to $ln(k_H^A) + 0.5$ and $ln(k_H^A) - 0.5$ respectively. The baseline depth of the Ringold lower mud layer boundary is 78 m. In the numerical experiment design, the depth is allowed to vary from 70-90 meters based on the stratigraphic unit information from nearby boreholes (Thorne *et al.*, 2006; Williams *et al.*, 2008; USDOE, 2010).

3.2.3 Hydrostatic pressure assumption

Traditionally, for subsurface flow simulations, the pressure on the river bed (P_{RB}) is assumed to be equal to the hydrostatic pressure (P_H). While the actual pressure on the river bed (P_{RB}) is deviated from the hydrostatic pressure (P_H) because of the surface water fluid dynamics. In this study, effects of the deviation (P_H-P_{RB}) on the net hyporheic exchange are investigated. To obtain P_{RB} from the CFD model, we spun up the surface water flow to an equilibrium steady state for each selected flow condition, then the pressure on the river bed (P_{RB}) is solved based on Eqs. (1) and (2). The simulated VOF field (i.e., the surface water stage) was then kept frozen at the equilibrium state, while setting the velocities to zero as well as changing the upstream and downstream boundaries to impermeable walls. The surface water domain is spun up again with the frozen VOF field and zero velocity to a converged state. This second spin-up provides us a new pressure distribution on the river bed, which can be considered as the hydrostatic pressure (P_H) that has exactly the same surface water stage distribution as the case with a dynamic flow field. The differences in pressure fields on the riverbed and simulated hyporheic fluxes for these two cases were compared, and the results will be discussed in Section 4.2. The impacts from the assumption of hydrostatic pressure were quantitatively compared with subsurface properties' uncertainty, and the results will be discussed in Section 4.2 as well.

3.2.4 Methodology for sensitivity measurements

For addressing all the uncertainties mentioned above, we constructed one control case and seven experiments (experiments A to G) as listed in Table III. In each experiment, the hyporheic fluxes

318 are simulated across the river bed and the estimated net hyporheic exchange rate integrated over
319 the entire domain is calculated. Response functions between the net fluxes and the river discharge
320 and inland water level can be constructed empirically using a 1st order polynomial function by
321 minimizing the least squares of errors (Björck, 1996; Rao *et al.*, 1999) for each experiment. These
322 functions are then be used to estimate time series of the hyporheic exchange for the period of 2008
323 to 2014 where no gaps exist in the historical records.

324

325 With the results for all the numerical experiments including the control case, analysis of variance
326 (ANOVA) based on a generalized linear model (GLM) regression was employed to quantitatively
327 measure the importance of the three perturbed parameters and the assumption of hydrostatic
328 pressure (Anscombe, 1948; Box, 1954; McCullagh and Nelder, 1989; Chambers and Hastie, 1992;
329 Pan *et al.*, 2013; Bao *et al.*, 2015). Assuming the response variable Y follows a normal
330 distribution, a GLM is fitted with the following model:

$$Y_i = c_0 + \sum_{j=1\ to\ J} c_j x_{i,j} + \varepsilon_i, \quad (10)$$

331 where $x_{i,j}$ represents the ith realization of the jth parameter, which are in the original forms of the
332 selected factors, or their linear or nonlinear transformed formats to represent first or higher order
333 terms, or two-way interactions via multiplication; c_j is the fitted coefficient for the jth parameter
334 that can be estimated by minimizing the mean square of errors; and ε is model-fitting residuals. In
335 this study, two response variables Y are investigated. One is the mean net hyporheic flux on the 7-
336 km river bed in the period of 2008 to 2014, and another one is the distance $D_{e,c}$ from the
337 Kolmogorov-Smirnov test (K-S test) (Kolmogorov, 1933; Smirnov, 1948) of the net hyporheic
338 flux on the 7-km river bed in the period of 2008 to 2014. $D_{e,c}$ represents the distance between two
339 CDFs, and is calculated as:

$$D_{e,c} = sup|F_e - F_c|, \quad (11)$$

where F_e is the CDF of the simulated net hyporheic flux time series in the period of 2008 to 2014 from numerical experiments with perturbed parameters, F_c is the CDF of the predicted net hyporheic flux time series in period of 2008 to 2014 from the control case, and sup represent supremum function. Parameter values used in all numerical experiments are listed in Table III. The simulated net hyporheic flux time series are derived from the response model trained by the CFD simulation results for the 50 randomly selected flow conditions (Table II). The details about this response model is introduced in Section 4.2.

Generally, use of a GLM is recommended for a monotonic system (Tong, 2009), and it can offer an explicit equation to present the relationship between input and output parameters, which is favorable for engineering applications (Pan *et al.*, 2013). ANOVA is a collection of statistical models used to analyze the regression models. The relative importance of each parameter is quantified by comparing the original regression model with the ones by removing the parameter from the explanatory variables. The reduction in the total explained variance indicates the importance of the corresponding parameter.

4. Results

Before the implementation of the numerical experiments and sensitivity analysis, the proposed CFD model was validated with on-site measurements and survey. As introduced in Section 2, for validating the CFD simulation results in the surface water domain, an ADCP survey was done on 19th February 2016. The CFD simulation results match ADCP very well. More details about the comparison between CFD simulation and ADCP survey are discussed in supplementary material.

For validating the CFD simulation results in the subsurface domain, five iButtons were installed on the river bed, whose locations are marked as red triangles in Figure 1(a). The CFD simulations can capture the hyporheic flux variations at the five iButtons for different flow conditions very well. The method for measuring hyporheic flux by iButtons and results comparison are discussed in separate papers (Zhou *et al.*, 2017a; Zhou *et al.*, 2017b) and summarized in the supplementary material.

4.1 Sensitivity analysis of hyporheic exchanges

The validated CFD model then was used to study the hyporheic flux on the river bed for combinations of different flow conditions, subsurface properties, and hydrostatic pressure assumption as discussed in Section 3.2 and listed in Table III. Hyporheic fluxes on the river bed for the control case with No. 5, 3, 23, and 21 flow conditions are shown in Figure 4(a) to (d). The No. 5 flow condition has the lowest river water discharge in the selected 50 flow conditions, No. 3 has the highest river water discharge in the selected 50 flow conditions, No. 23 has the highest net hyporheic flux into river, and No. 21 has the highest net hyporheic flux into subsurface. It is noticeable that the magnitudes of hyporheic fluxes are relatively larger near the shore, and relatively smaller in the middle of the river. This is mainly caused by the large aspect ratio of the domain geometry. The river is around 800 m wide, the permeable subsurface layers (alluvium, Hanford, and Ringold gravel) are totally around 30 m. Therefore, surface water near the shore can relatively easier flow in or out the large subsurface domain at the two sides of the river. However, water in the middle of the river has to travel through the 30 m deep, a few hundred meters wide subsurface channel before reaching the bank. Hyporheic fluxes on the river bed for the control case for all the 50 flow conditions are shown in Figure S4 in supplementary materials. Figure 4(e)

and (h) shows stream lines in the subsurface on the cross section A-A (marked in Figure 4(a)) for flow conditions No. 5, 3, 23, and 21 as well. The red portion of streamlines represents water flows upward into the surface water, and blue portion stands for the streamlines flow downward into the subsurface. The green line is the water level in the subsurface domain. There is almost no water exchange between the permeable layers (Hanford and Ringold gravel layers) and non-permeable layer (Ringold lower mud layer) as expected. For No. 5 and 23 flow conditions (Figure 4(e) and (g)), water flows from the subsurface into river, because of the low river water discharge and high inland water level. For No. 3 and 21 flow conditions (Figure 4(f) and (h)), water tends to flow strongly from river into the subsurface, because of the high river water discharge and low inland water level. It worth mentioning that the streamlines are three-dimensional, so the streamlines look not very continuous or smooth when it is shown on a two-dimensional cross section. The vertical direction in Figure 4(e) to (h) is scaled up eight times to show the streamlines clearly.

Figure 5 shows the hyporheic flux differences (Δf) between the experiments with perturbed parameters and the control case. Δf is calculated as:

$$\Delta f = f_e - f_c, \tag{12}$$

where f_e is the flux from the numerical experiments and f_c is the flux form the control case for the flow condition No. 3. The flow condition No. 3 leads to strong fluxes flowing into the subsurface. Therefore, in Figure 5, warmer colors means that the perturbed parameters decrease the hyporheic flux, and cold colors stand for enhanced hyporheic fluxes. For experiments A and B (Figure 5(a) and (b)), which adjust the thickness of alluvium layer, a thinner alluvium layer (1 m) leads to an increase in the hyporheic exchange (Figure 5(a)), and a thicker alluvium layer (3 m) results in a

406 decrease in the flux (Figure 5(b). In experiments C and D (Figure 5(c) and (d)), the upper boundary
407 of Ringold lower mud layer was adjusted. For the experiment C (Figure 5(c)), the upper boundary
408 is at 70 m, and it leads to a higher flux because the relative thicker permeable layer between the
409 river bed and the Ringold lower mud layer. While a narrower permeable layer leads to a smaller
410 flux when the upper boundary is at 90 m in experiment D (Figure 5(d)). Experiments E and F
411 adjust the permeability in the alluvium layer. For the permeability adjusted to $k_H^A \times 1.648$, which
412 is equivalent to $ln(k_h^A) + 0.5$, the flux is larger than that from the control case (Figure 5(e)). For
413 the permeability adjusted to $k_H^A/1.648$, which is equivalent to $ln(k_h^A) - 0.5$, the flux is smaller
414 than that from the control case (Figure 5(f)). Experiment G (Figure 5(g)) uses the hydrostatic
415 pressure as the boundary condition for the subsurface domain. There is no clear trend of decreasing
416 or enhancing the hyporheic flux.

417

418 Figure 6 shows the net hyporheic fluxes over the 7-km river bed for the 50 selected flow conditions
419 in the seven experiments compared with the fluxes from the control case (red line). The impacts
420 from the perturbed parameters are consistent with the hyporheic flux distribution on the river bed
421 under the No. 3 flow condition as shown in Figure 5. Generally, experiments A, C, and E enhance
422 the hyporheic flux. Experiments B, D and F decrease the hyporheic fluxes. For experiment G, it
423 shows that estimated hyporheic flux is almost the same as the control case, which means that the
424 assumption of applying hydrostatic pressure as the boundary condition is reasonable over the
425 historical period.

426

According to the 50 selected cases, the net hyporheic exchange rate on the river bed of the study domain can be empirically related to the river discharge and inland water stage by constructing a 1st order polynomial function (Eq.(13)) for the control case and each experiment. Eq. (13) demonstrates an empirical function for the control case with a R^2 of 0.8.

$$Q_Z = -0.002356Q_R + 4.998h - 519.5, \quad (13)$$

where Q_Z is the net hyporheic exchange (m^3/s) on the river bed over the study domain, Q_R is the river discharge (m^3/s), and h is the inland water stage (m). Using the constructed empirical function (Eq. (13)), the net hyporheic discharge Q_Z over the study domain in the period of 2008 to 2014 were estimated based on historical inland water stage data measured from inland well (as shown in Figure 1(a)) and river discharge data. The time series of Q_Z is shown in Figure S5 in supplementary materials, and interested readers can refer to Zhou et al. (Zhou *et al.*, 2017b). The constructed empirical functions were then used to estimate the net hyporheic flux for the corresponding experiments for the period from 2008 to 2014. The mean net hyporheic exchange in the 7-km river reach of the control case and seven experiments over the study period are listed in Table III. The CDFs of the time series of net hyporheic exchange rates for the numerical experiments (i.e., experiments A to G) are shown in Figure 7. The blue lines in Figure 7 are the CDFs for the control case, and the red lines are the CDFs for the parameter perturbation experiments. The distance $D_{e,c}$ from the K-S test was used to measure the differences of the CDFs between the control case and the experiments A to G as shown in Figure 7. The distances $D_{e,c}$ are listed in Table III. By comparing the CDFs, the thickness of alluvium layer has the most significant impact on the hyporheic flux (experiments A and B), the permeability of the alluvium layer is also important to the hyporheic flux (experiments E and F), because the alluvium layer is the interface between the river water and subsurface domain, which is expected to affect the flux considerably.

449 The Ringold lower mud layer upper boundary can slightly impact the hyporheic flux (Experiments
450 C and D), because the 70 to 90 m range of the upper boundary of Ringold lower mud layer, which
451 represents stratigraphic unit information from nearby boreholes (Thorne *et al.*, 2006; Williams *et*
452 *al.*, 2008; USDOE, 2010) in the study domain, is still very small compared to the ~800 m wide
453 river. The assumption of using the hydrostatic pressure as the boundary condition (Experiment G)
454 leads to almost the same CDF as that from the control case. The qualitative comparison among the
455 CDF indicates that the three subsurface property and structure parameters are more important than
456 the assumption of hydrostatic pressure for averaged fluxes over the domain, but such an analysis
457 does not give us quantitative information on the importance among the three subsurface property
458 and structure parameters.

459

460 To quantify the relative importance of the parameters, the ANOVA method based GLM regression
461 described in Section 3.2.4 was used to measure their impacts using two metrics: the mean net
462 hyporheic exchanges and distance $D_{e,c}$ from the K-S test. For the ANOVA, the inputs are the four
463 perturbed parameters (column 2 to 5 in Table III), and the output is the mean hyporheic exchanges
464 on the river bed and distance $D_{e,c}$ (column 6 and 7 in Table III). Figure 8 shows the sensitivity
465 scores of the four parameters for the two response variables (i.e., the mean net hyporheic flux and
466 the distance $D_{e,c}$). Consistent with the qualitative investigation on the hyporheic flux distribution
467 on the river bed for flow condition No.3 (Figure 5), net hyporheic flux or the 50 selected flow
468 conditions (Figure 6) and CDFs (Figure 7), the alluvium layer thickness shows significant
469 importance based on both response variables, which contributes about 75% of the total variance in
470 terms of both metrics. Alluvium layer permeability and Ringold lower mud layer upper boundary
471 contribute around 10% to the total variance respectively, and the alluvium layer permeability is

slightly more important than that of the Ringold lower mud layer in modulating the exchange. The assumption of using the hydrostatic pressure as the boundary condition is the least important parameter, which contributes around 0.8% and 4% for the mean net hyporheic flux and distance $D_{e,c}$ based sensitivity measures, respectively.

4.2 Impacts of hydrostatic pressure assumption on the hyporheic exchanges

Sensitivity analyses discussed in Section 4.2 show that the assumption of applying hydrostatic pressure almost has the least impact on the net hyporheic flux on the 7-km river bed. Figure 9(a) shows the pressure difference ($P_\Delta = P_H - P_{RD}$) on river bed by using the No. 5 flow condition in Table II. The mean of P_Δ is -2.2 Pa, and the standard deviation is 14.9 Pa. Figure 9(b) shows the difference of local hyporheic fluxes ($\Delta f = f_H - f_{RD}$) on river bed between two cases with P_H and P_{RD} applied on the river bed as pressure boundary conditions. The mean of flux difference is 1.97×10^{-8} m s^{-1}, and the standard deviation of flux difference is 3.24×10^{-7}m s^{-1}. The mean hyporheic fluxes from 2008 to 2014 on the 7-km river bed are -0.642 m^3 s^{-1} and -0.643 m^3 s^{-1} for applying P_{RD} and P_H as pressure boundary conditions respectively. This means that by considering fluid dynamics, the mean net hyporheic flux that penetrates into the subsurface is about 0.16% more. Therefore, this indicates that the surface water fluid dynamics do not significantly impact the net hyporheic flux on the whole 7-km river bed. However, if the study domain is smaller, such as a river section of a few hundred meters, the impact from the considering fluid dynamics may be larger. Figure 9(c) shows the boxplot for the relationship between selected domain area and relative difference in mean net fluxes defined as:

$$F_{\Delta r} = \frac{F_H - F_{RD}}{|F_{RD}|}. \quad (14)$$

where F_{RD} is the net hyporheic flux averaged over the period of 2008 to 2014 in a selected sub-domain with P_{RD} as the boundary condition, and F_H is its counterpart with P_H as the boundary condition. To draw robust conclusions, we generated ten thousand sub-domains with random positions and sizes for this analysis. For the sub-domain area smaller than 1.6 km^2, the relative difference $F_{\Delta r}$ can be over $\pm 10\%$. For the sub-domain area larger than 2.4 km^2, $F_{\Delta r}$ is controlled smaller than $\pm 1\%$. The total river bed area of the 7-km river is about 4.7 km^2. This is consistent with the general understanding that the hydrostatic assumption is sufficient for large river reaches.

5 Conclusion

A one way coupled river surface water and subsurface three-dimensional CFD simulation model was built in the commercial CFD software STAR-CCM+. Through validations against data from an ADCP survey for the surface water flow, and a one-month long iButton survey for the hyporheic fluxes, the proposed CFD model can provide reliable results for a large scale (a few km) river reach, and the computation cost is affordable with parallel computations. Each flow condition requires around a simulation of 6-10 hours for stabilizing the surface water flow on 96 CPU cores on the PNNL Institutional Computing (PIC) cluster using Intel Haswell E5-2670 CPUs (Intel, 2012). Each subsurface parameter setup requires a simulation of ~1 hour on the same computing cluster. The proposed CFD model was applied to explore the impact of alluvium layer thickness, alluvium layer permeability, Ringold lower mud layer upper boundary, and the assumption of hydrostatic pressure. Generally, a thinner alluvium layer, a larger permeability, and a lower Ringold lower mud layer upper boundary lead to larger hyporheic fluxes across the river bed. The

514 results from the numerical experiments were then used to construct empirical functions that relate
515 the hyporheic flux to river discharge and inland water stage, which are applied to estimate the
516 mean hyporheic flux and CDF for the period from 2008 to 2014 over the study domain. Based on
517 the estimated net hyporheic flux, the CDFs and the ANOVA-based sensitivity analysis, we
518 demonstrate that the alluvium layer thickness has the biggest impact on the hyporheic exchange,
519 followed by the alluvium layer permeability and the upper boundary depth of the Ringold lower
520 mud layer, while the assumption of hydrostatic pressure shows the least impact for a 7-km section
521 river reach. To our knowledge, this is the first quantitative study on comparing the uncertainty
522 induced by the assumption of hydrostatic pressure with that by subsurface structure and properties
523 uncertainty. Though the uncertainty induced by hydrostatic pressure assumption is relatively small
524 for the 7-km river reach, our detailed statistical analysis based on random samples from the domain
525 shows that, for the studied section of the Columbia river, when the sub-domain area is smaller than
526 1.6 km^2, the relative difference $F_{\Delta r}$ can be more than $\pm 10\%$. For the sub-domain area larger than
527 2.4 km^2, $F_{\Delta r}$ is smaller than $\pm 1\%$.

528

529 This study shows a good example and application to use the proposed CFD model combined with
530 uncertainty quantification tools to study hyporheic exchange in a large river reach with frequent
531 hydropeaking events. However, although the three-dimensional CFD model is useful for studying
532 such exchanges for at multiple snapshots under selected flow conditions, the model is
533 computationally expensive and can hardly be extended for continuous simulations, since the CFD
534 simulation needs sub-second time step interval to reach converged solutions. Therefore, we will
535 explore means to improve the computational efficiency of the modeling framework, such as using
536 the open source CFD tools open-FOAM (Jiang and Liu, 2017; OpenCFD, 2017; Zhou *et al.*, 2017),

to alleviate limitations imposed by commercial software (i.e., a license is required for each CPU for STAR-CCM+ applications) in the near future.

6 Acknowledgements

This research was supported by the U.S. Department of Energy (DOE), Office of Biological and Environmental Research (BER), as part of BER's Subsurface Biogeochemistry Research Program (SBR). This contribution originates from the SBR Scientific Focus Area (SFA) at the Pacific Northwest National Laboratory (PNNL). The computation resources were provided and supported by PNNL Institutional Computing (PIC). The authors also thank Sara Niehus for providing MASS1 simulation supports.

Reference

Anderson JK, Wondzell SM, Gooseff MN, Haggerty R. 2005. Patterns in stream longitudinal profiles and implications for hyporheic exchange flow at the H.J. Andrews Experimental Forest, Oregon, USA. Hydrol. Process., **19**: 2931–2949. DOI: 10.1002/hyp.5791.

Anscombe FJ. 1948. The Validity of Comparative Experiments. J. R. Stat. Soc. Series A, **111**: 181-211.

Arntzen EV, Geist DR, Dresel PE. 2006. Effects of fluctuating river flow on groundwater/surface water mixing in the hyporheic zone of a regulated, large cobble bed river. River Res. Appl., **22**: 937–946. DOI: 10.1002/rra.947.

Banda MK, Seaid M. 2012. Lattice Boltzmann simulatin for shallow water flow applications. In: Hydrodyanmics - Theory and Model, Jin HZ (ed.) In Tech.

Bao J, Hou Z, Huang M, Liu Y. 2015. On approaches to analyze the sensitivity of simulated hydrologic fluxes to model parameters in the Community Land Model. Water, **7**: 6810–6826. DOI: 10.3390/w7126662.

Bao J, Schaefer L. 2013. Lattice Boltzmann equation model for multi-component multi-phase flow with high density ratios. Applied Mathematical Modelling, **37**: 1860-1871.

Björck Å. 1996. Numerical Methods for Least Squares Problems.

Box GEP. 1954. Some Theorems on Quadratic Forms Applied in the Study of Analysis of Variance Problems, I. Effect of Inequality of Variance in the One-Way Classification. Annals of Mathematical Statistics, **25**: 290-302.

Brunke M, Gonser T. 1997. The ecological significance of exchange processes between rivers and groundwater. Freshw. Biol., **37**: 1-33. DOI: 10.1046/j.1365-2427.1997.00143.x.

CD-adapco. 2015. STAR-CCM+ 10.04 User Guide. CD-adapco.

Chambers JM, Hastie TJ. 1992. Statistical Models in S., Chapman and Hall/CRC.

Chen X, Glenn H, Murray C, Rockhold M, V V, Zachara J. 2013. Application of ensemble-based data assimilation techniques for aquifer characterization using tracer data at Hanford 300 area. Water Resources Research, **49**.

Chen X, Murakami H, Hahn M, Glenn H, Rockhold M, Zachara J, Rubin Y. 2012. Three-dimensional Bayesian geostatistical aquifer characterization at the Hanford 300 Area using tracer test data. WATER RESOURCES RESEARCH, **48**: W06501.

Coleman A, Larson K, Ward D, Lettrick J. 2010. Development of a High-Resolution Bathymetry Dataset for the Columbia River through the Hanford Reach. Pacific Northwest National Laboratory.

Constantinescu G, Koken M, Zeng J. 2011. The structure of turbulent flow in an open channel bend of strong curvature with deformed bed: insight provided by detached eddy simulation. Water Resources Research, **47**: W05515.

Donath S, Feichtinger C, Pohl T, Gotz J, Rude U. 2010. A paralle free surface lattice Boltzmann method for large-scale applications. In: Parallel Computational Fluid Dynamics: Recent Advances and Furture Directions, Biswas R (ed.) DEStech Publications Inc.

Findlay S. 1995. Importance of surface-subsurface exchange in stream ecosystems: the hyporheic zone. Limnology and Oceanography, **40**: 159-164.

Findlay S, Strayer D, Goumbala C, Gould K. 1993. Metabolism of streamwater dissolved organic carbon in the shallow hyporheic zone. Limnol. Oceanogr., **38**: 1493–1499. DOI: 10.4319/lo.1993.38.7.1493.

Fritz BG, Arntzen EV. 2007. Effect of rapidly changing river stage on uranium flux through the hyporheic zone. Ground Water, **45**: 753-760.

Fritz BG, Arntzen EV. 2007. Effect of rapidly changing river stage on uranium flux through the hyporheic zone. Ground Water, **45**: 753–760. DOI: doi:10.1111/j.1745-6584.2007.00365.x.

Fritz BG, Mackley R, Khon N, Patton G, Gilmore T, Mendoza D, McFarland D, Bunn A, Arntzen E. 2007. Investigation of the hyporheic zone at the 300 Area, Hanford Site. PNNL-16805. Richland, Washington: Pacific Northwest National Laboratory.

Hanasaki N, Kanae S, Oki T. 2006. A reservoir operation scheme for global river routing models. J. Hydrol., **327**: 22–41. DOI: 10.1016/j.jhydrol.2005.11.011.

Hancock RJ. 2002. Human Impacts on the Stream-Groundwater Exchange Zone. Environmental Management, **29**: 763-781. DOI: 10.1007/s00267-001-0064-5.

Hartman MJ, Dresel PE. 1998. Hanford site groundwater monitoring for fiscal year 1997, Rep. PNNL-11793.

Huang H, Ayoub J. 2006. Applicability of the Forchheimer Equation for Non-Darcy Flow in Porous Media. SPE Journal: 112-122.

Intel. 2012. Intel® Xeon® Processor E5-2670.

Jiang Y, Liu X. 2017. Experimental and numerical investigation of density current over macro-roughness. Environmental Fluid Mechanics. DOI: 10.1007/s10652-016-9500-1.

Jongen T. 1998. Simulation and Modeling of Turbulent Incompressible Flows. École polytechnique fédérale de Lausanne.

Kalbus EF, Reinstorf F, Schirmer M. 2006. Measuring methods for groundwater, surface water and their interactions: a review. Hydrol. Earth Syst. Sci. Discuss., **3**: 1809–1850. DOI: 10.5194/hessd-3-1809-2006.

Kazemi E, Tait S, Shao S, Nichols A. 2016. Potential application of mesh-free SPH method in turbulent river flow. In: Hydrodyanmic and Mass Transport at Freshwater Aquatic Interfaces, Rowinski PM, Marion A (eds.) Springer.

Keylock CJ, Constantinescu G, Hardy RJ. 2012. The application of computational fluid dynamics to natural river channels: eddy resolving versus mean flow approaches. Geomorphology, **179**: 1-20.

Kolmogorov A. 1933. Sulla determinazione empirica di una legge di distribuzione. G. Ist. Ital. Attuari., **4**: 83–91.

Lane SN, Bradbrook KF, Richards KS, Biron PA, Roy AG. 1999. The application of computational fluid dyanmics to natural river channels: three-diemsional versus two-dimensional approaches. Geomorphology, **29**: 1-20.

Liu CC, Ferng YM, Shih CK. 2012. CFD evaluation of turbulence models for flow simulation of the fuel rod bundle with a spacer assembly. Applied Thermal Engiineering, **40**: 389-396.

McCullagh P, Nelder J. 1989. Generalized Linear Models. Second Edition Edn., Boca Raton.

McMichael GA, Perkins WA, McMurray CJ, chien YJ, rakowski CL, Coleman A, Richmond MC, vucelick J, Arntzen EV, Mueller RP, duberstein CA, Lukas J. 2003. Subyearling Chinook Salmon Stranding in the Hanford Reach of the Columbia River. In: PNWD-3308, Preparedfor Grant County Public Utility District No. 2 by Battelle Pacic Northwest Division, Richland, Washington.

Newcomb RC, Brown SG. 1961. Evaluation of bank storage along the Columbia River between Richland and China Bar. In: Washington. US Govt. Print. Off.

Newcomb RC, Strand J, Frank F. 1972. Geology and ground-water characteristics of the Hanford Reservation of the US Atomic Energy Commission. In: Washington. US Govt. Print. Off.

Niehus SE, Perkins WA, Richmond MC. 2014. Simulation of Columbia River Hydrodynamics and Water Temperature from 1917 through 2011 in the Hanford Reach. In: Rep. PNWD-3278 (p. 148). Battelle-Pacific Northwest Division, Richland, Washington.

O.Reynolds. 1895. On the Dynamical Theory of Incompressible Viscous Fluids and the Determination of the Criterion. Philosophical Transactions of the Royal Society of London, **186**: 123-164.

OpenCFD. 2017. OpenFOAM user guide.

Pan W, Bao J, Lo C, Lai K, Agarwal K, Koeppel B, Khaleel M. 2013. A general approach to develop reduced order models for simulation of solid oxide fuel cell stacks. Journal of Power Sources, **232**: 139-151.

Poff NL, Allan JD, Bain MB, Karr JR, Prestegaard KL, Richter BD, Sparks RE, Stromberg JC. 1997. The Natural Flow Regime: A paradigm for river conservation and restoration N. Bioscience, **47**: 769–784. DOI: 10.2307/1313099.

Rao CR, Toutenburg H, Fieger A, Heumann C, Nittner T, Scheid S. 1999. Linear Models: Least Squares and Alternatives. In: Springer Series in Statistics, Springer.

Richmond MC, Perkins WA. 2009. Efficient Calculation of Dewatered and Entrapped Areas Using Hydrodynamic Modeling and GIS. Environmental Modelling & Software, **24**: 1447-1456. DOI: 10.1016/j.envsoft.2009.06.001

Schmitt FG. 2007. About Boussinesq's turbulent viscosity hypothesis: historical remarks and a direct evaluation of its validity. Comptes Rendus Mécanique, **335**: 617-627.

Shih TH, Liou WW, Shabbir A, Yang ZG, Zhu J. 1995. A new k-epsilon eddy viscosity model for high Reynolds number turbulent flow. Comput Fluids, **24**: 227-238.

Smirnov N. 1948. Table for estimating the goodness of fit of empirical distributions. Annals of Mathematical Statistics, **19**: 279–281. DOI: 10.1214/aoms/1177730256.

Sobczak WV, Findlay S. 2002. Variation in bioavailability of dissolved organic carbon among stream hyporheic flowpaths. Ecology, **83**: 3194–3209. DOI: 10.2307/3071853.

Thorne PD, Bergeron MP, Williams MD, Freedman VL. 2006. Groundwater data package for Hanford assessments. PNNL-14573, Rev, **1**.

Tiffan KF, Garland RD, Rondorf DW. 2002. Quantifying flow-dependent changes in subyearling fall chinook salmon rearing habitat using two-dimensional spatially explicit modeling. North American Journal of Fisheries Management, **22**: 713-726.

Tong C. 2009. PSUADE User's Manual.

Turcotte DL, Schubert G. 1982. Geodynamics: Applications of Continuum Physics to Geological Problems. John Wiley & Sons.

USDOE. 2010. Hanford Site Groundwater Monitoring and Performance Report for 2009: Volumes 1 & 2. DOE/RL-2010-11.

Valett HM, Morrice JA, Dahm CN, Campana ME. 1996. Parent lithology, surface-groundwater exchange, and nitrate retention in headwater streams. Limnol. Oceanogr., **41**: 333–345. DOI: 10.4319/lo.1996.41.2.0333.

Vandersteen G, schneidewind U, Anibas C, Schmidt C, Seuntjens P, batelaan O. 2015. Determining groundwater-surface water exchange from temperature-time series: Combining a local polynomial method with amaximum likelihood estimator. Water Resources Research, **51**: 922–939. DOI: 10.1002/2014WR015829.Received.

Versteeg HK, Malaasekera W. 1995. An introduction to computational fluid dynamics: the finite volume method. Wiley.

Vörösmarty CJ, Sahagian DL. 2000. Anthropogenic disturbance of the terrestrial water cycle. Bioscience, **50**: 753–765.

Williams MD, Rockhold ML, Thorne PD, Chen Y. 2008. Three-dimensional groundwater models of the 300 Area at the Hanford Site, Washington State. Pacific Northwest National Laboratory (PNNL), Richland, WA (US).

Winter TC. 1999. Relation of streams, lakes, and wetlands to groundwater flow systems. Hydrogeol. J., **7**: 28-45. DOI: 10.1007/s100400050178.

Wolfstein M. 1969. The velocity and temperature distribution in one-dimensional flow with turbulence augmentation and pressure gradient. International Journal of Heat and Mass Transfer, **12**: 301-318.

688 Yazdi J, Sarkardeh H, Azamathulla HM, Ghani AA. 2010. 3D simulation of flow around a single spur dike
689 wih free-surface flow. International Journal of River Basin Management, **8**: 55-62.
690 Zachara JM, Freshley MD, Last GV, Peterson RE, Bjornstad BN. 2012. Updated Conceptual Model for the
691 300 Area Uranium Groundwater Plume. Pacific Northwest National Laboratory (PNNL), Richland,
692 WA (US).
693 Zarnetske JP, Haggerty R, Wondzell SM, Baker MA. 2011a. Dynamics of nitrate production and removal
694 as a function of residence time in the hyporheic zone. J. Geophys. Res. Biogeosciences, **116**: 1–
695 12. DOI: 10.1029/2010JG001356.
696 Zarnetske JP, Haggerty R, Wondzell SM, Baker MA. 2011b. Labile dissolved organic carbon supply limits
697 hyporheic denitrification. J. Geophys. Res. Biogeosciences, **116**. DOI: 10.1029/2011JG001730.
698 Zhou T, Bao J, Huang M, Hou Z, Arntzen E, Mackley R, Harding S, Murray C, Perkins W, Chen X, Stegen J,
699 Hammond G, Thorne P, Zachara J. 2017b. Quantifying hyporheic exchange dynamics in a highly
700 regulated large river reach. Water Resources Research, **Under review**.
701 Zhou T, Endreny TA. 2013. Reshaping of the hyporheic zone beneath river restoration structures: Flume
702 and hydrodynamic experiments. water Resources Research, **49**: 5009-5020.
703 Zhou T, Huang M, Bao J, Hou Z, arntzen E, Mackley R, Crump A, Goldman A, Song X, Xu Y, Murray C,
704 Stegen J, Zachara J. 2017a. Spatial and temporal variations in shallow water hyporheic
705 exchanges along a highly regulated large river reach. Groundwater, **Under review**.
706 Zhou T, Nijssen B, Gao H, Lettenmaier DP. 2016. The contribution of reservoirs to global land surface
707 water storage variations. J. Hydrometeorol., **150923131555009**. DOI: doi:10.1175/JHM-D-15-
708 0002.1.
709 Zhou Z, Hsu TJ, Cox D, Liu X. 2017. Large-eddy simulation of wave-breaking induced turbulent coherent
710 structures and suspended sediment transport on a barred beach. Journal of Geophysical
711 Research. DOI: 10.1002/2016JC011884.

712

Table I. Subsurface properties for the control case.

	Horizontal permeability (m^2)		Ratio between the vertical and horizontal permeability		porosity
Alluvium layer	Heterogeneous	(k_H^A)	0.1	(k_V^A/k_H^A)	0.170
Hanford layer	1.23×10^{-8}	(k_H^H)	0.1	(k_V^H/k_H^H)	0.373
Ringold gravel layer	1.93×10^{-9}	(k_H^{RG})	0.35	(k_V^{RG}/k_H^{RG})	0.294
Ringold lower mud layer	2.527×10^{-15}	(k_H^{RM})	0.27	(k_V^{RG}/k_H^{RG})	0.351

Table II. The 50 river discharge and inland water level conditions used as boundary conditions for the numerical experiments.

Flow condition index	River discharge (m^3/s)	Upstream stage (m)	Upstream velocity (m/s)	Downstream stage (m)	Inland well water stage (m)	Inland upstream stage (m)	Inland downstream stage (m)
1	3041.0	105.7208	1.156667	104.8642	104.8591	105.3871	104.5351
2	2309.7	105.3217	0.978750	104.7200	104.9220	105.4500	104.5980
3	8651.2	108.8004	1.779167	107.4263	107.7089	108.2369	107.3849
4	3823.3	106.2621	1.263750	105.3033	105.5156	106.0436	105.1916
5	1132.1	104.7954	0.568750	104.6108	104.7711	105.2991	104.4471
6	6613.1	107.8425	1.588333	106.6000	106.6478	107.1758	106.3238
7	5163.6	107.0417	1.445417	105.8954	106.3290	106.8570	106.0050
8	1815.3	105.0938	0.810417	104.6788	104.8743	105.4023	104.5503
9	3405.1	106.0871	1.169167	105.2767	105.3969	105.9249	105.0729
10	3299.5	106.0413	1.152500	105.2625	105.5000	106.0280	105.1760
11	3547.1	106.1133	1.220417	105.2254	105.1885	105.7165	104.8645
12	4455.1	106.6358	1.358750	105.5746	105.7603	106.2883	105.4363
13	2223.3	105.3388	0.943333	104.7917	105.0504	105.5784	104.7264
14	2025.0	105.1454	0.897917	104.6358	104.9222	105.4502	104.5982
15	1754.5	105.1733	0.782083	104.8163	104.9467	105.4747	104.6227
16	3679.1	106.2117	1.231250	105.3133	105.2486	105.7766	104.9246
17	3024.6	105.8492	1.104167	105.1146	105.1840	105.7120	104.8600
18	4642.7	106.8329	1.356250	105.8308	105.9540	106.4820	105.6300
19	4294.1	106.6179	1.310417	105.6538	105.9451	106.4731	105.6211
20	2364.3	105.5029	0.948750	104.9617	105.3559	105.8839	105.0319
21	6310.8	107.7854	1.532083	106.6550	106.5015	107.0295	106.1775
22	3222.3	105.9400	1.150833	105.1379	105.2405	105.7685	104.9165
23	2824.3	105.6571	1.087917	104.9125	105.4675	105.9955	105.1435
24	2361.7	105.4267	0.961250	104.8546	104.9886	105.5166	104.6646
25	4362.8	106.6525	1.326250	105.6738	106.2739	106.8019	105.9499
26	3788.8	106.3829	1.217083	105.5471	105.3687	105.8967	105.0447
27	2127.4	105.3417	0.888750	104.8621	104.9636	105.4916	104.6396
28	2517.2	105.5471	0.989167	104.9496	105.1534	105.6814	104.8294
29	1916.2	105.1413	0.850417	104.6933	105.0291	105.5571	104.7051
30	3790.9	106.2100	1.274167	105.2229	105.2280	105.7560	104.9040
31	2130.4	105.3238	0.899583	104.8321	104.9651	105.4931	104.6411
32	4826.2	106.9188	1.384583	105.8733	105.9191	106.4471	105.5951
33	3518.4	106.1675	1.186250	105.3421	105.4175	105.9455	105.0935
34	2043.6	105.2021	0.895417	104.7046	104.8760	105.4040	104.5520
35	4100.2	106.4775	1.291250	105.5183	105.5210	106.0490	105.1970
36	7940.8	108.4708	1.722917	107.1292	107.5395	108.0675	107.2155
37	2802.5	105.6100	1.077500	104.8779	104.9983	105.5263	104.6743
38	3570.5	106.1546	1.204583	105.2838	105.6315	106.1595	105.3075
39	6141.1	107.5767	1.547917	106.3467	106.6117	107.1397	106.2877
40	2483.8	105.5017	0.986667	104.8979	105.1674	105.6954	104.8434
41	2927.9	105.8213	1.072083	105.1292	105.3053	105.8333	104.9813
42	3856.0	106.2963	1.267500	105.3442	105.6352	106.1632	105.3112
43	2267.3	105.3863	0.944167	104.8408	105.0380	105.5660	104.7140
44	1804.8	105.1183	0.811667	104.7188	104.8361	105.3641	104.5121
45	1798.8	104.8133	0.904167	104.2929	104.5712	105.0992	104.2472
46	5021.1	107.0354	1.405000	105.9746	105.9160	106.4440	105.5920
47	5412.7	107.1767	1.474583	106.0038	106.2098	106.7378	105.8858
48	5336.4	107.1625	1.457083	106.0229	106.2567	106.7847	105.9327
49	2688.9	105.5867	1.052083	104.8979	105.0307	105.5587	104.7067
50	2864.7	105.6838	1.100833	104.9300	105.0992	105.6272	104.7752

Table III. Summary of numerical experiments for sensitivity analysis on subsurface properties and riverbed pressure boundary conditions; P_{RD} * is the actual pressure considering river water fluid dynamics; P_H** is the hydrostatic pressure.

	Alluvium layer thickness (m)	**Alluvium layer permeability (m^2)**	**Ringold lower mud layer upper boundary (m)**	**Pressure on river bed**	**Mean net hyporheic flux on the river bed (m^3/s)**	**Distance between CDFs ($D_{e,c}$)**
Control	2	Estimated from underwater video-camera footage and accompanying grain-size analyses (k_H^A)	78	P_{RD}*	-0.642	0.000
Exp. A	1	k_H^A	78	P_{RD}	-0.998	0.160
Exp. B	3	k_H^A	78	P_{RD}	-0.569	0.045
Exp. C	2	k_H^A	70	P_{RD}	-0.680	0.031
Exp. D	2	k_H^A	90	P_{RD}	-0.539	0.077
Exp. E	2	$k_H^A \times 1.648$	78	P_{RD}	-0.754	0.067
Exp. F	2	$k_H^A / 1.648$	78	P_{RD}	-0.557	0.064
Exp. G	2	k_H^A	78	P_H**	-0.643	0.003

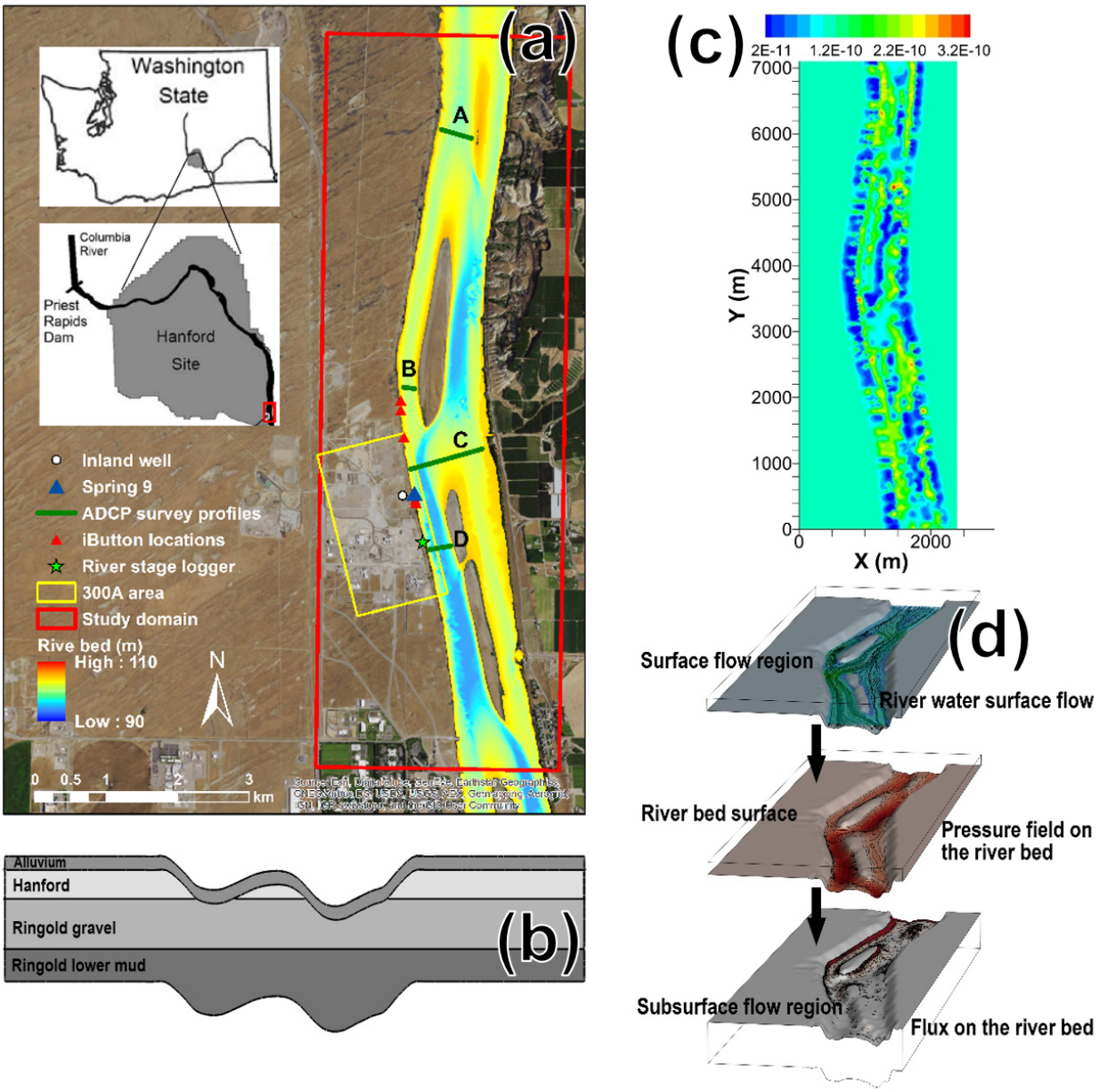

Figure 1: Configurations of the studied river reach; (a) Studied 7-km Columbia River domain; (b) Sketch of the layered subsurface structure (not draw in scale); (c) Horizontal permeability distribution in alluvium layer (k_H^A); (d) Sketch of the one-way coupling frame

(a)

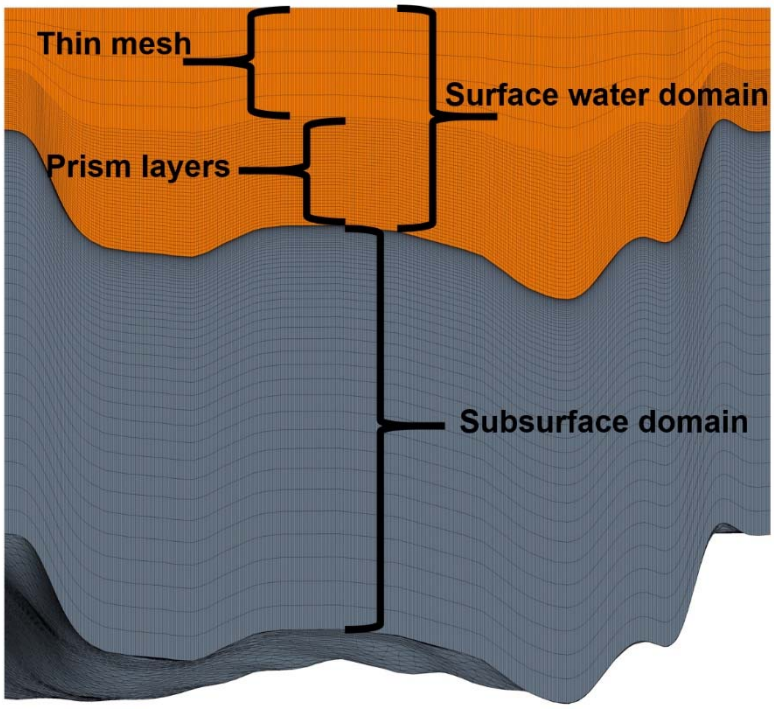

(b)

Figure 2: Meshes for the simulation domain. (a) Perspective view of the meshes; (b) side view of the meshes for clarifying the mesh regions. For showing the mesh clearly, the vertical direction (z) is scaled up 10 times.

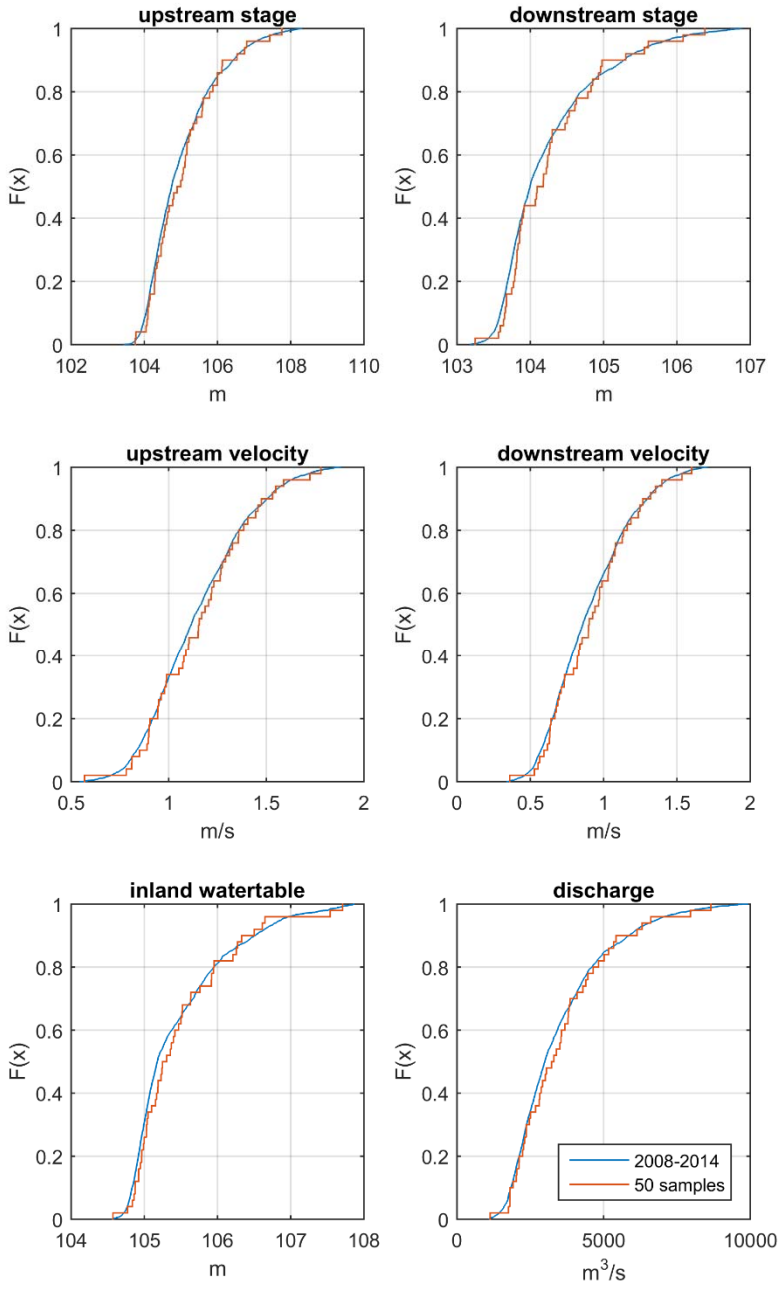

Figure 3: Comparison between the cumulative density functions of the MASS1 outputs from 2008 to 2014 and the 50 selected flow conditions used as boundary conditions for the CFD simulations.

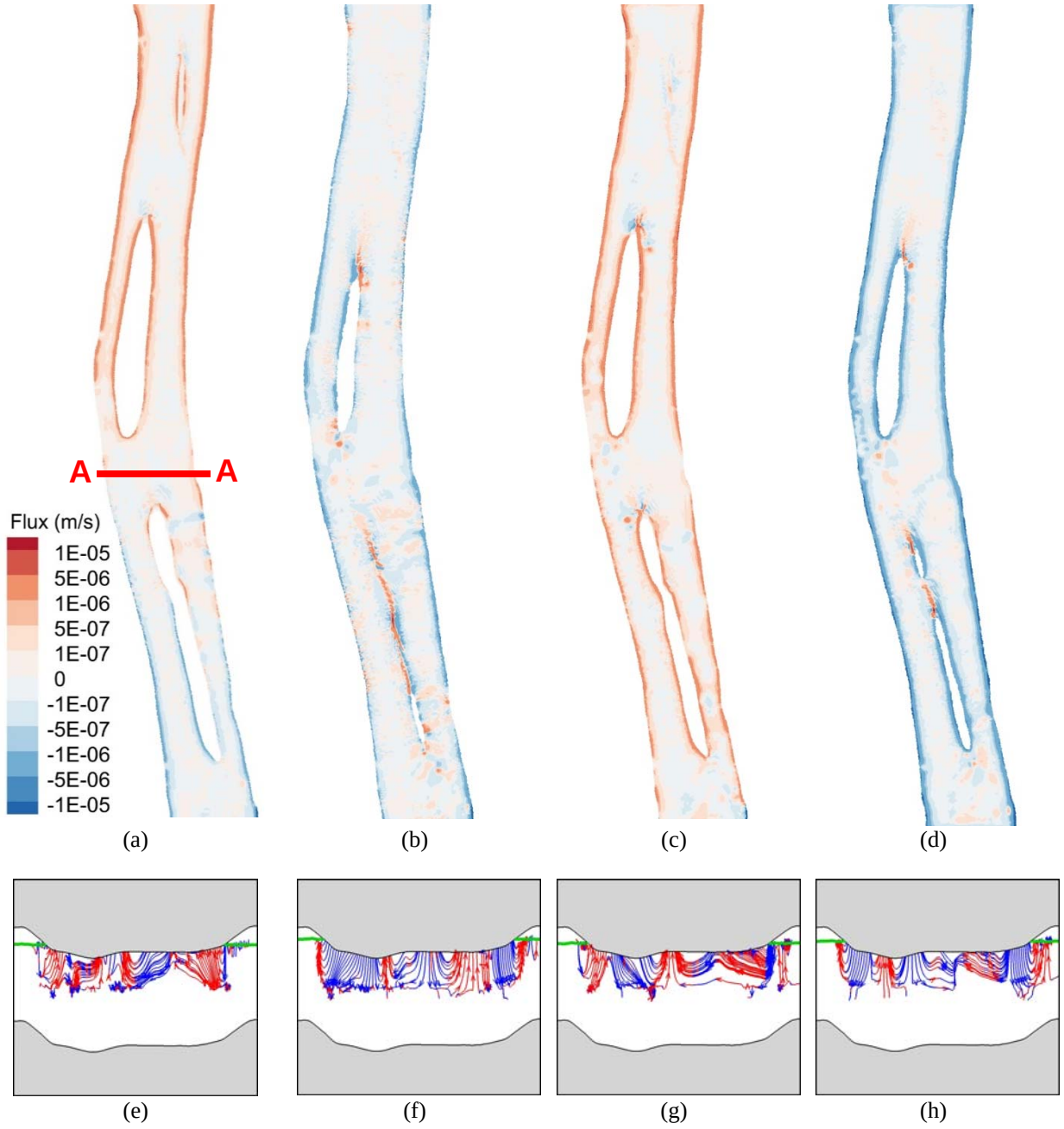

Figure 4: Hyporheic fluxes on the river bed, and stream lines at cross section A-A (red line in Figure 6(a)). (a) Hyporheic fluxes on river bed under the No. 5 flow condition (i.e., the lowest river discharge). The warm color means the flux flows into river surface water, and the cold color means the flux flows into subsurface; (b) Hyporheic fluxes on river bed under the No. 3 flow condition (i.e., the highest river discharge); (c) Hyporheic fluxes on river bed under the No. 23 flow condition (i.e., the highest net hyporheic flux into river); (d) Hyporheic fluxes on river bed under the No. 21 flow condition (i.e., the highest net hyporheic flux into subsurface); (e) streamlines at cross section A-A under the No.5 flow condition. The red portion means the stream flow upward into river surface water, and the blue portion means the stream flow downward into subsurface. Green line is the water level; (f) streamlines at cross section A-A under the No.3 flow condition; (g) streamlines at cross section A-A under the No.23 flow condition; (h) streamlines at cross section A-A under the No.21 flow condition.

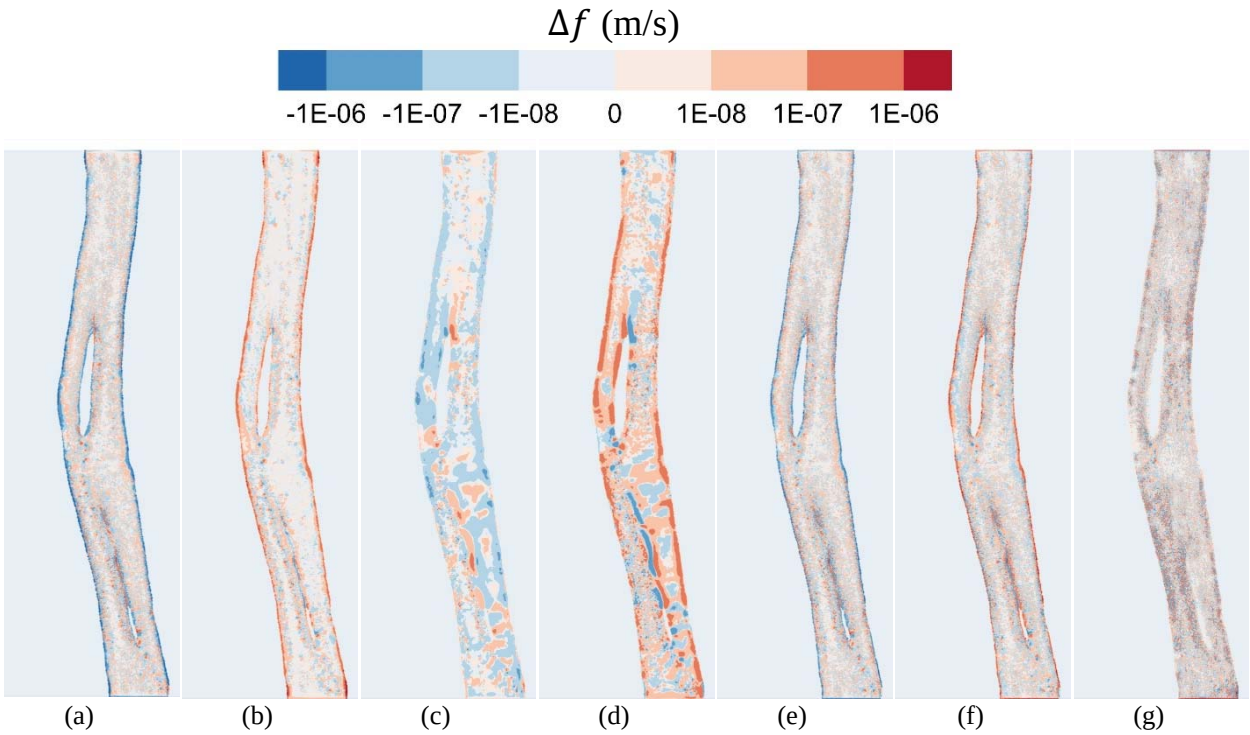

Figure 5: Difference in hyporheic fluxes between the experiments with perturbed parameters and the control case for the flow condition No. 3 (i.e., the highest river discharge), and (a)-(g) stand for the experiments A to G.

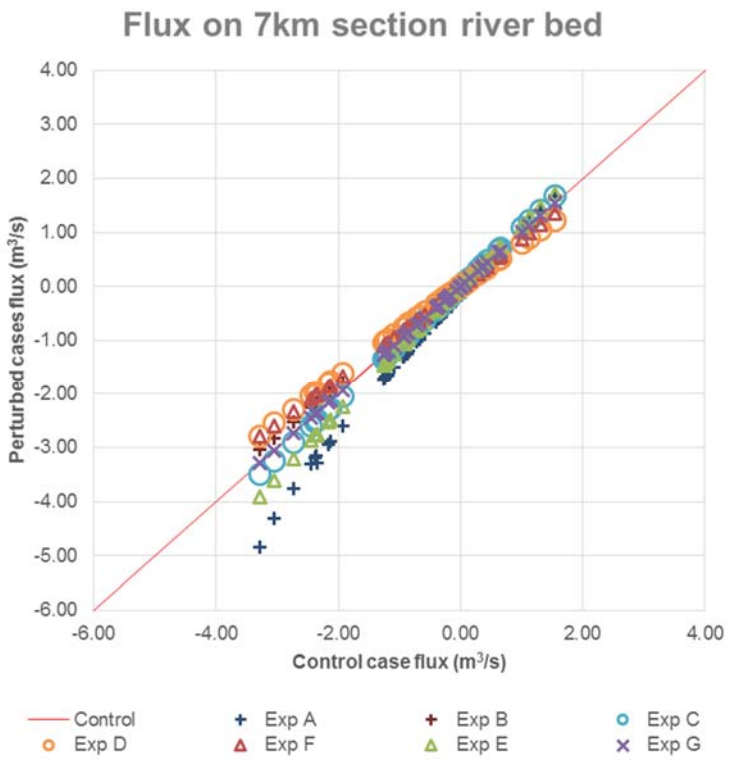

Figure 6: Net hyporheic fluxes on the 7-km river bed for the 50 selected flow conditions from the seven experiments compared with the flux from control case (red line).

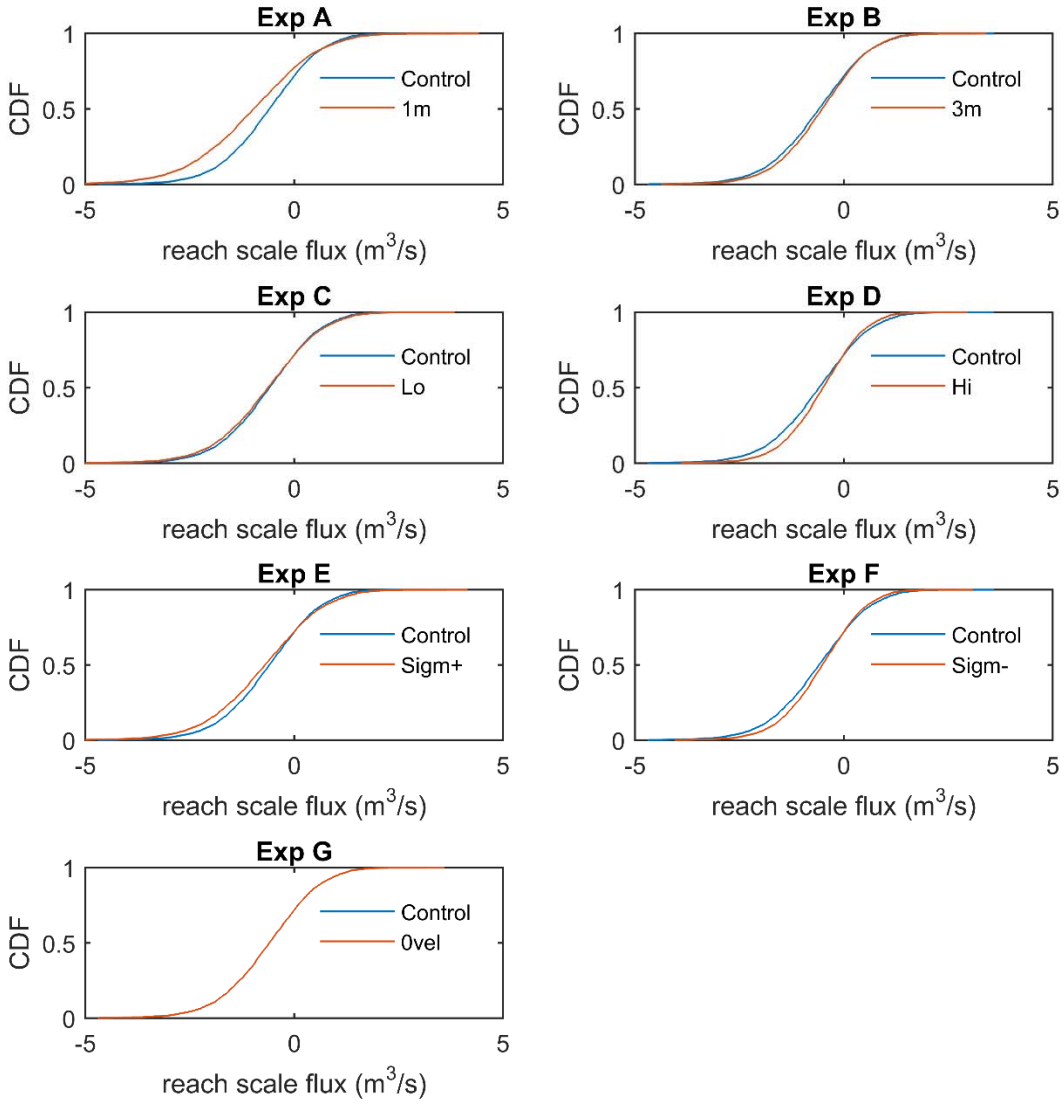

Figure 7: The CDFs of net hyporheic exchange rates on the river bed of the study domain in the period from 2008 to 2014 for the parameter perturbation experiments A to F.

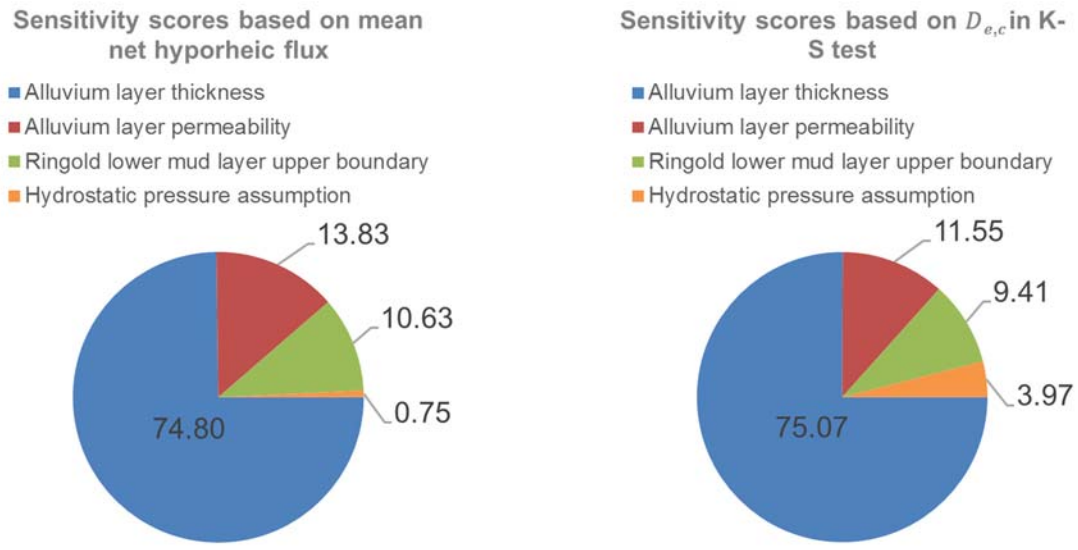

(a) (b)

Figure 8: Sensitivity scores for perturbed parameters and model setups. (a) Sensitivity scores based on the mean net hyporheic flux; (b) Sensitivity scores based on the $D_{e,c}$ in the K-S test.

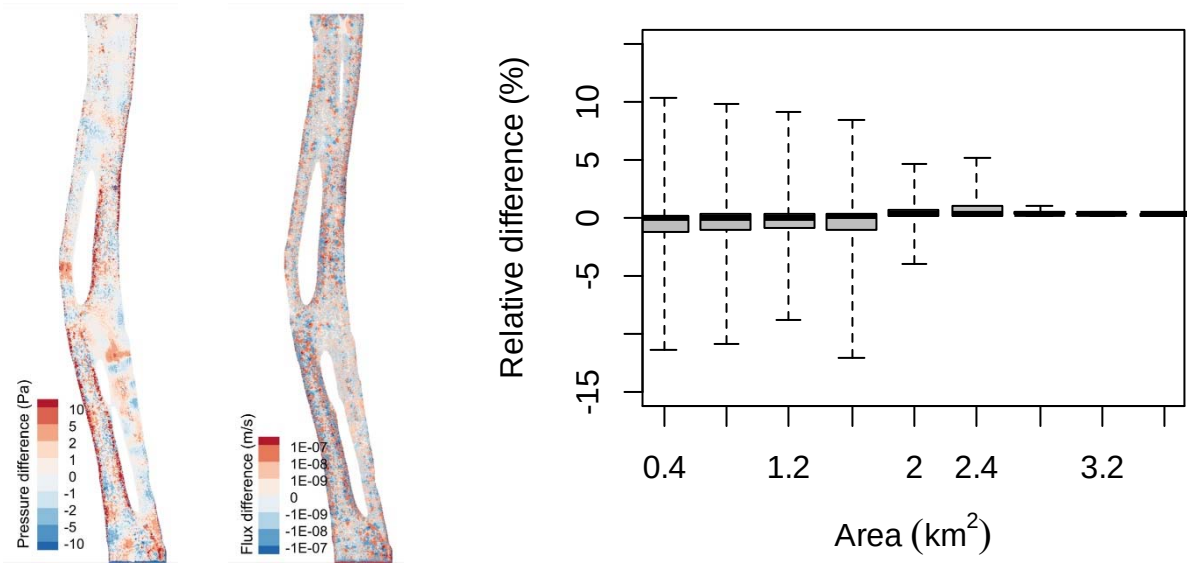

(a) (b) (c)

Figure 9: Difference between the cases with and without considering surface water dynamic pressure. (a) Pressure difference (P_Δ); (b) Hyporheic flux difference on river bed; (c) boxplot for the relationship between domain size (i.e., in terms of area) and relative difference in the net hyporheic flux.

Supplementary Materials

Quantifying Hyporheic Exchanges in a Large Scale River Reach Using Coupled 3-D Surface and Subsurface Computational Fluid Dynamics Simulations

J. Bao[1], T. Zhou[1], M. Huang[1], Z. Hou[1], W. Perkins[1], S. Harding[1], S. Tizler[1], G. Hammond[2], H. Ren[1], P. Thorne[1], S. Suffield[1], C. Murray[1], J. Zachara[1], T. Scheibe[1]

[1]Pacific Northwest National Laboratory, Richland, WA, USA

[2]Sandia National Laboratories, Albuquerque, NM, USA

S.1 Surface water flow validation

As introduced in Section 2, for validating the CFD simulation results in the surface water domain, an ADCP survey was done on 19 Febuary 2016. On the ADCP survey day, the daily averaged upstream river water stage is 105.6 m, and the averaged velocity is 1 m s^{-1}, which are used for the inlet boundary. The downstream river water stage is 105.04 m, which is used as the outlet boundary combining with the hydrostatic pressure. Upstream stage, downstream stage, and the inlet velocity are derived from MASS1 modeling. Figure S1(a) shows the CFD simulated velocity profiles and stream lines for the flow conditions on the ADCP survey day. With two islands, the river water mainly enters the east channel to cross the north island, and then turns west into the west channel to cross the south island.

Because the ADCP survey cannot measure the local elevation of the river water surface, the CFD simulated surface water stages averaged over transects corresponding to the MASS1 nodes are compared against MASS1 calculated stages, as shown in Figure S1(b). The CFD results can capture the river stage gradient fairly well. Figure S1(c) shows the comparison of CFD simulated river water discharge with ADCP measurements at each cross section as marked in Figure 1(a). The CFD results can match the measurements very well. Figure S2 shows the velocity profiles comparison between CFD simulated result and ADCP measurements at cross sections A to D. The figures in the left column are the velocity magnitude vs. depth profiles at 1/6, 1/3, 1/2, 2/3, and 5/6 width of the cross sections. The figures in the right column are the velocity profiles on the whole cross section. The CFD simulation results match ADCP very well, with only slight deviations. There are a few reasons that may cause the small deviations. Firstly, the CFD simulations used the daily averaged flow condition as the boundary conditions, but the ADCP measure the velocity at

each location for 15 seconds, so the flow condition kept changing during the ADCP survey. Secondly, the comparing location shown in Figure 4 may not be the exactly same, because of the limitation of boat's location and elevation accuracy and the CFD geometry accuracy. Finally, the CFD geometry cannot capture every details on the river bed, such as small stones, plants and moving objects in the river.

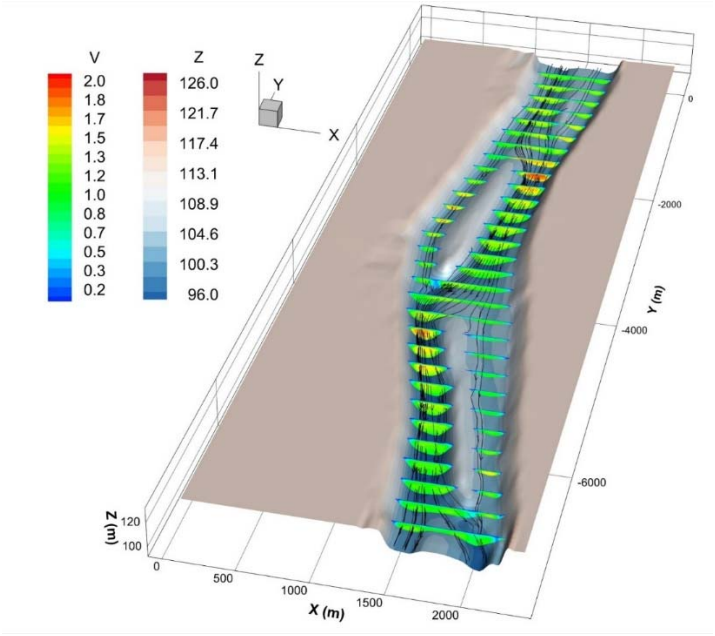

(a)

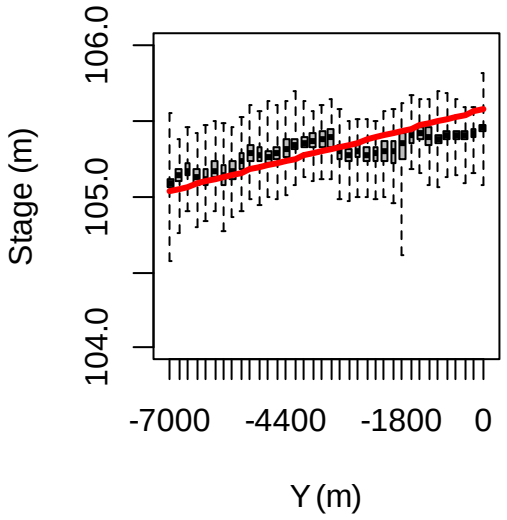

(b)

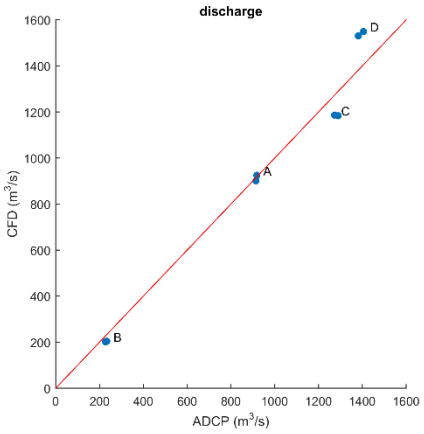

(c)

Figure S1: CFD simulation results and validation; (a) CFD simulated velocity profiles and stream lines for the flow condition on ADCP survey day; (b) Comparison between CFD simulated stages with MASS1calculated stages; (c) Comparison between CFD simulated river water discharges with ADCP measured ones.

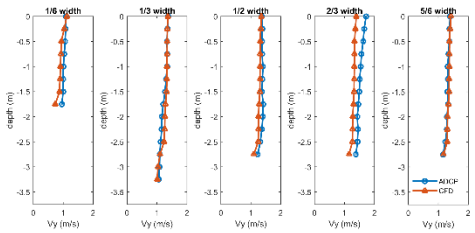

Cross section A
(a)

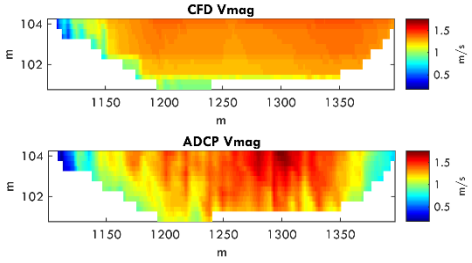

Cross section A
(b)

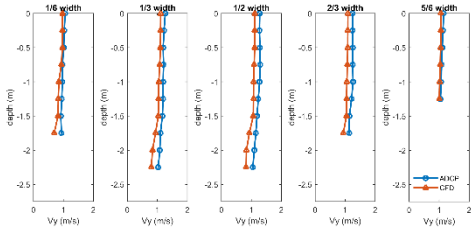

Cross section B
(c)

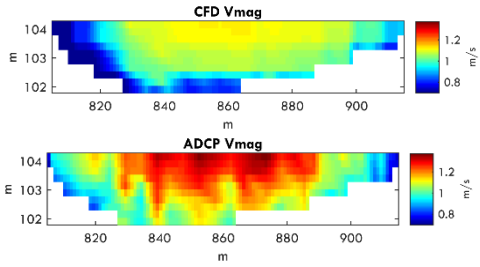

Cross section B
(d)

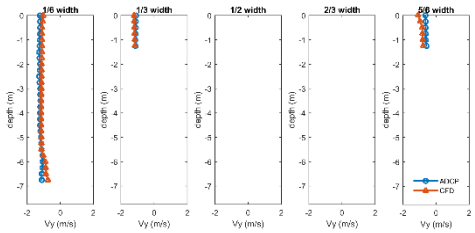

Cross section C
(e)

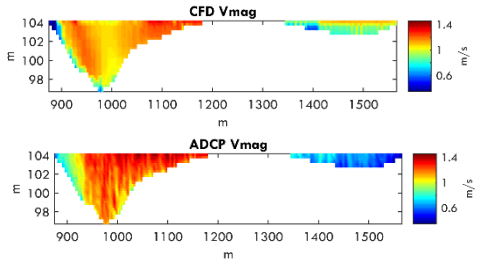

Cross section C
(f)

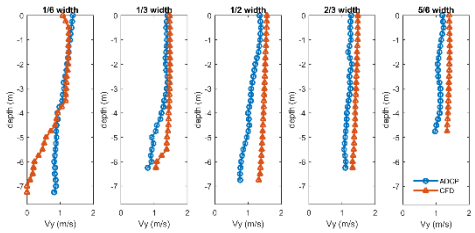

Cross section D
(g)

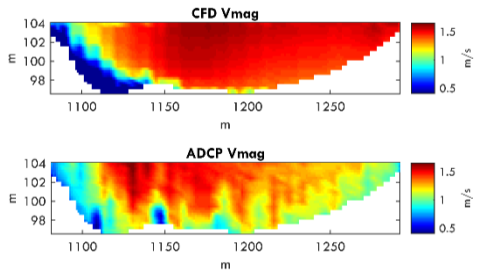

Cross section D
(h)

Figure S2: Comparison between CFD simulated velocity profiles with ADCP measurements at cross sections A to D as marked in Figure 1(a). The left column (a), (c), (e), and (g) are the velocity magnitude vs. depth profiles at 1/6, 1/3, 1/2, 2/3, and 5/6 width of the cross sections. The right column (b), (d), (f), and (h) shows the velocity magnitude on the whole cross section.

S.2 Hyporheic flux validation

The iButtons recorded the temperature profile at different depths in subsurface in March 2016. The temperature time series were then converted to hyporheic fluxes using a hybrid modeling framework (Zhou *et al.*, 2017b) that combines the dynamic harmonic regression (DHR) (Young *et al.*, 1999), an analytical solution (Turcotte and Schubert, 1982), and the Local Polynomial method with a Maximum Likelihood estimator (LPML) model (Vandersteen *et al.*, 2015). During the one month measuring period, three surface water flow conditions were selected to set up the CFD simulations. As marked in Figure S1(a), the three surface water flow conditions represent the low, median and high flow in March 2016. With the corresponding inland water stage as the orange line shown in Figure S1(a), the flux distributions on river bed for the three flow conditions are shown in Figure S1(b-d). The cold color means the river water penetrates into subsurface, and the warm color means the water flow back into the river. Figure S1(e) shows the comparison of hyporheic fluxes between the CFD simulations and iButtons measurements. The lines are the CFD simulated flux along the red line marked in Figure S1(b), and the bars are the iButtons measurements at the five locations as the red stars marked in Figure S1(b) or the red triangles marked in Figure 1.

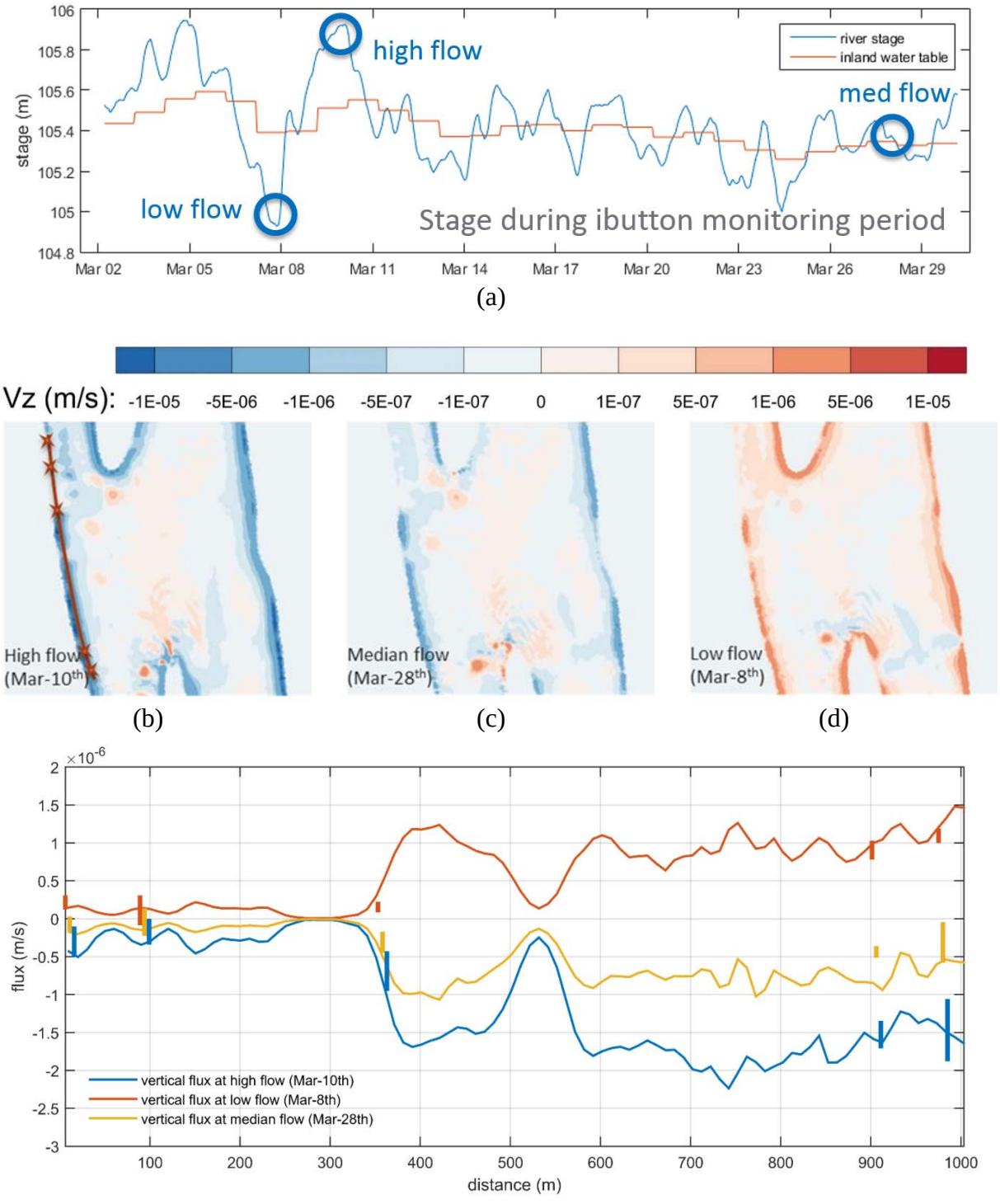

Figure S3: Comparison of hyporheic flux on the river bed between the CFD simulations and iButton measurements. (a) Flow conditions and inland water stage during the iButton measurement period; (b-d) CFD simulated hyporheic fluxes on the river bed for the low, median, and high flow conditions. (e) Comparison of hyporheic fluxes alone the red line in panel (b) between the CFD simulations and iButton measurements.

S.3 Hyporheic fluxes on the river bed

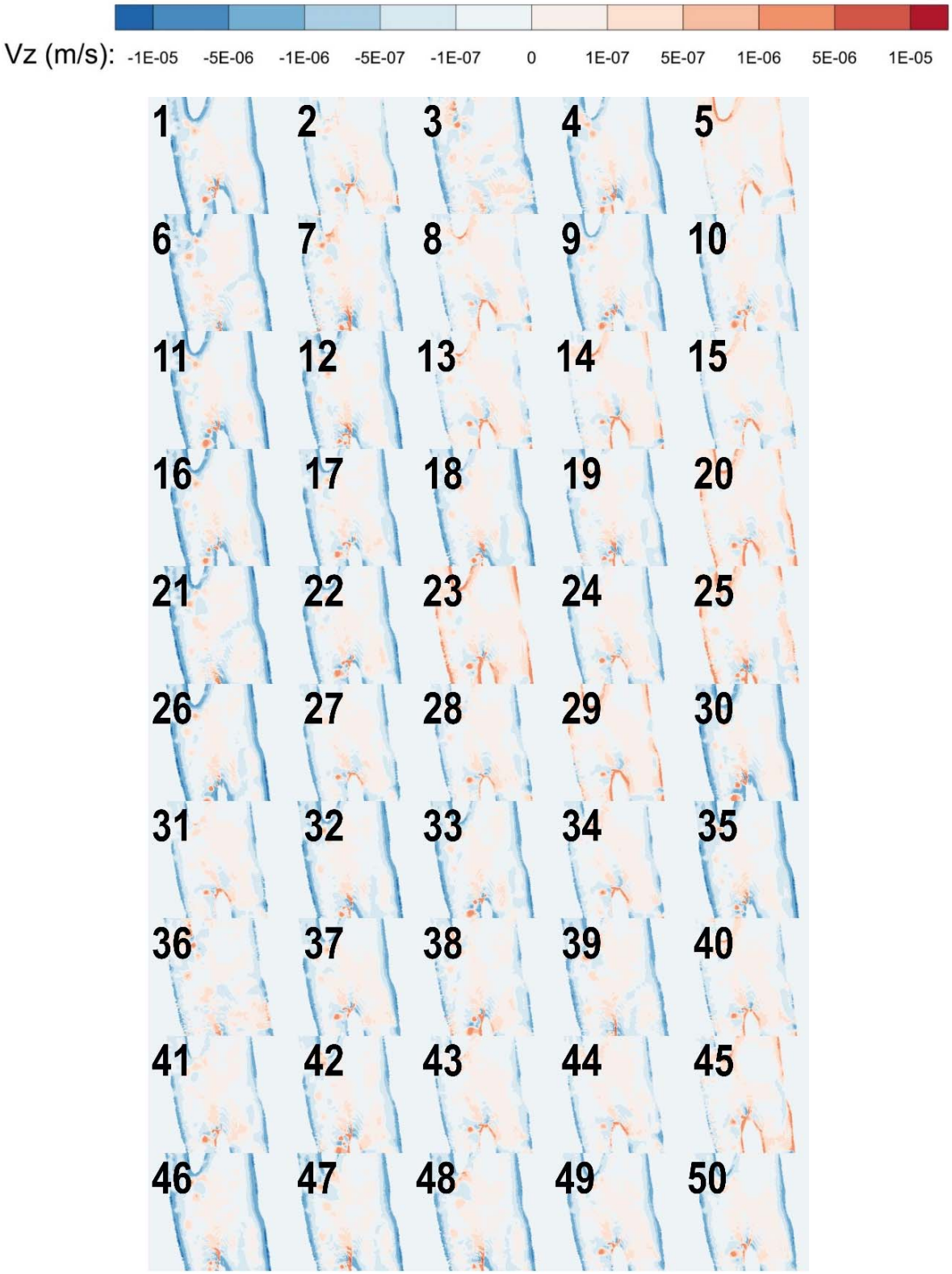

Figure S4: Hyporheic fluxes on the river bed for the control case under the 50 selected flow conditions.

S.4 Time series of hyporheic exchanges on the river bed

The total hyporheic exchange on the river bed for the 7-km river reach is estimated by the regressed polynomial function:

$$Q_Z = -0.002356Q_R + 4.998h - 519.5, \quad \text{(S1)}$$

where Q_Z is the net hyporheic exchange (m^3/s) on the river bed of study domain, Q_R is the river discharge (m^3/s), and h is the inland water stage (m). Using the constructed empirical function in S1, the net hyporheic exchange Q_Z in the study domain over the 7-year period from 2008 to 2014 were estimated based on historical inland water stage data measured from inland well (as shown in Figure 1(a)) and river discharge data calculated from the MASS1 model. Figure S3 shows the time series of Q_Z, and more details are discussed in Zhou et al (Zhou *et al.*, 2017a; Zhou *et al.*, 2017b). The mean hyporheic exchange for the period 2008 to 2014 is -0.642 m^3/s.

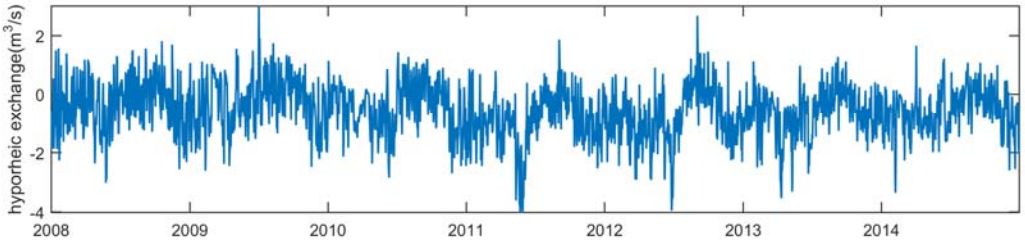

Figure S5: Time series of hyporheic exchange on the river bed of study domain.

Reference

Turcotte DL, Schubert G. 1982. Geodynamics: Applications of Continuum Physics to Geological Problems. John Wiley & Sons.

Vandersteen G, schneidewind U, Anibas C, Schmidt C, Seuntjens P, batelaan O. 2015. Determining groundwater-surface water exchange from temperature-time series: Combining a local polynomial method with amaximum likelihood estimator. Water Resources Research, **51**: 922–939. DOI: 10.1002/2014WR015829.Received.

Young PC, Pedregal D, Tych W. 1999. Dynamic harmonic regression. J. Forecast., **18**: 369–394. DOI: 10.1002/(SICI)1099-131X(199911)18:6<369::AID-FOR748>3.0.CO;2-K.

Zhou T, Bao J, Huang M, Hou Z, Arntzen E, Mackley R, Harding S, Murray C, Perkins W, Chen X, Stegen J, Hammond G, Thorne P, Zachara J. 2017b. Quantifying hyporheic exchange dynamics in a highly regulated large river reach. Water Resources Research, **Under review**.

Zhou T, Huang M, Bao J, Hou Z, arntzen E, Mackley R, Crump A, Goldman A, Song X, Xu Y, Murray C, Stegen J, Zachara J. 2017a. Spatial and temporal variations in shallow water hyporheic exchanges along a highly regulated large river reach. Groundwater, **Under review**.